JGR Oceans

Key Points:

- Moored instrumentation allows for prolonged time series of turbulence estimates with concurrent in-situ meteorological and wave measurements
- Law of the Wall and Monin-Obukhov Similarity theory are able to predict measurements of ε in certain turbulence regimes
- In the context of turbulence scaling, it may be unnecessary to distinguish between a wind-driven and Langmuir-driven turbulence regime

Correspondence to:

U. K. Miller,
ukm2103@columbia.edu

Scaling of Moored Surface Ocean Turbulence Measurements in the Southeast Pacific Ocean

Una Kim Miller[1] , Christopher J. Zappa[1] , Seth F. Zippel[2] , J. Thomas Farrar[2] , and Robert A. Weller[2]

[1]Lamont-Doherty Earth Observatory, Columbia University, Palisades, NY, USA, [2]Woods Hole Oceanographic Institution, Falmouth, MA, USA

Abstract Estimates of turbulence kinetic energy (TKE) dissipation rate (ε) are key in understanding how heat, gas, and other climate-relevant properties are transferred across the air-sea interface and mixed within the ocean. A relatively new method involving moored pulse-coherent acoustic Doppler current profilers (ADCPs) allows for estimates of ε with concurrent surface flux and wave measurements across an extensive length of time and range of conditions. Here, we present 9 months of moored estimates of ε at a fixed depth of 8.4 m at the Stratus mooring site (20°S, 85°W). We find that turbulence regimes are quantified similarly using the Obukhov length scale (L_M) and the newer Langmuir stability length scale (L_L), suggesting that ocean-side friction velocity (u_*) implicitly captures the influence of Langmuir turbulence at this site. This is illustrated by a strong correlation between surface Stokes drift (u_s) and u_* that is likely facilitated by the steady Southeast trade winds regime. In certain regimes, $\frac{u_*^3}{\kappa z}$, where κ is the von Kármán constant and z is instrument depth, and surface buoyancy flux capture our estimates of ε well, collapsing data points near unity. We find that a newer Langmuir turbulence scaling, based on u_s and u_*, scales ε well at times but is overall less consistent than $\frac{u_*^3}{\kappa z}$. Monin-Obukhov similarity theory (MOST) relationships from prior studies in a variety of aquatic and atmospheric settings largely agree with our data in conditions where convection and wind-driven current shear are both significant sources of TKE, but diverge in other regimes.

Plain Language Summary Surface ocean turbulence is key to the transfer of heat, gas, and other climate-relevant properties between the ocean and atmosphere. Because turbulence is difficult to measure in the field, it is often parameterized using more easily obtained variables such as wind speed, wave measurements, and surface heat flux. Here, we test such parameterizations against an extensive time series of turbulence measurements collected on a mooring line attached to a surface buoy in the Southeast Pacific Ocean. This region is known to support important South American fisheries as well play a significant role in the global radiation budget, yet is poorly represented in climate models. We find the parameterizations to describe our measurements well, and we explore how conditions at the study site influence their performance.

1. Introduction

Turbulence kinetic energy (TKE) drives the mixing of heat, momentum, and gases within and between the ocean and atmosphere, making it an important parameter in studies of weather and climate. In the Ocean Boundary Layer (OBL), the region of the upper ocean defined by nearly uniform density and active vertical mixing, it is generated primarily by wind, waves, and buoyant convection and lost through viscous dissipation into heat. Production can generally be assumed to equal dissipation and thus the rate of TKE dissipation (ε) serves as a means for quantifying turbulence in a system.

Measurements of ε are difficult to make in the field and we rely instead on parameterizations for ε based on the TKE production terms that it balances. Such parameterizations have been traditionally developed using Monin-Obukhov similarity theory (MOST), a form of dimensional analysis applied to the boundary layers of the atmosphere and ocean (Monin & Obukhov, 1959) with which ε can be scaled using wind stress and surface buoyancy flux. The lack of an explicit wave scaling in MOST, however, puts into question its applicability to the OBL, where wave breaking and Langmuir turbulence can be leading sources of TKE. Langmuir turbulence, in particular, is thought to affect the OBL on a global scale and contribute to systematic biases in mixed layer depth and sea surface temperature in global climate models (Belcher et al., 2012). A new scaling framework that

Methodology: Una Kim Miller, Christopher J. Zappa, Seth F. Zippel, J. Thomas Farrar
Project Administration: Christopher J. Zappa, J. Thomas Farrar
Software: Una Kim Miller, Seth F. Zippel, J. Thomas Farrar
Supervision: Christopher J. Zappa, J. Thomas Farrar
Visualization: Una Kim Miller
Writing – original draft: Una Kim Miller
Writing – review & editing: Una Kim Miller, Christopher J. Zappa, Seth F. Zippel, J. Thomas Farrar, Robert A. Weller

accounts for Langmuir turbulence was proposed in Belcher et al. (2012), but the sparsity of ε measurements, especially with concurrent wave spectra, has limited its validation in the field.

Here, we examine the application of MOST and the Langmuir turbulence framework of Belcher et al. (2012) to explore the scaling of ε estimates obtained from a moored pulse-coherent acoustic Doppler current velocity profiler (ADCP). The ADCP was deployed on the "Stratus Mooring" (20°S, 85°W) as part of the Variability of American Monsoon Systems (VAMOS) Ocean–Cloud–Atmosphere–Land Study Regional Experiment (VOCALS-Rex) (Mechoso et al., 1995; Wood et al., 2011), a field campaign focused on the Southeast Pacific Ocean Stratus region. This region, named for its extensive stratus/stratocumulus cloud deck, plays an important role in the global radiation budget but is poorly understood and represented in global climate models (Lin, 2007; Ma et al., 1996; Mechoso et al., 1995; Richter, 2015; Zheng et al., 2011; Zuidema et al., 2016). This paper seeks to leverage the comprehensive and extensive turbulence data set made possible by the Stratus Mooring, which spans 9 months and a range of turbulent conditions, to contribute to our understanding of the OBL in this region. Notably, moored pulse-coherent ADCPs represent a new methodology for obtaining turbulence measurements (Zippel et al., 2021) that is especially well-suited for studies of turbulence scaling, as their moored configuration allows for the collection of concurrent, in-situ measurements of wind, waves, and surface fluxes.

2. Background

Assuming a horizontally homogeneous flow, the TKE budget may be written as

$$\frac{D\overline{e}}{Dt} = \underbrace{-\overline{\boldsymbol{u}_h'w'} \cdot \frac{\partial \boldsymbol{u}_h}{\partial z}}_{\substack{Shear \\ production}} - \underbrace{\overline{\boldsymbol{u}_h'w'} \cdot \frac{\partial \boldsymbol{u}_s}{\partial z}}_{\substack{Stokes \\ production}} + \underbrace{\overline{w'b'}}_{\substack{Buoyant\ production/ \\ destruction}} - \underbrace{\frac{\partial}{\partial z}\left(\overline{w'u_i'u_i'} + \frac{1}{\rho_0}\overline{w'p'}\right)}_{Transport} - \underbrace{\varepsilon}_{\substack{Destruction\ by\ viscous \\ dissipation}} \tag{1}$$

where e is TKE, $\boldsymbol{u}_h$ and w are horizontal and vertical velocities, $\boldsymbol{u}_s$ is the Stokes drift velocity vector, b is buoyancy ($b = -g\rho/\rho_0$), ρ and ρ_0 are density and background density, respectively, p is pressure, and z is depth, defined in the ocean as positive downward. Prime notation indicates the turbulent component of a Reynolds decomposed quantity, overbars indicate a time mean, and the subscript i indicates tensor notation. The shear production term describes TKE from the shear of currents generated by winds at the surface and the Stokes production term describes that of the shear of Stokes drift associated with surface waves. The interaction of Stokes drift with the shear of the wind-driven current results in Langmuir circulation, characterized by vertically-oriented, counter-rotating vortices that are often visible at the surface as streaks of foam or kelp aligned in the direction of the wind (Craik & Leibovich, 1976). These vortices result in enhanced turbulent vertical velocities that aid in the transport of TKE generated near the surface to the base of the mixed layer (Sutherland et al., 2014) and play an important role in the deepening of the mixed layer (Belcher et al., 2012; Li & Fox-Kemper, 2017). The transport term describes such vertical transport by turbulence-turbulence interactions. The buoyancy term describes the production of TKE by free convection associated with destabilizing surface buoyancy fluxes or its destruction by stratification caused by stabilizing fluxes. The final term and focus of this paper, ε, describes the conversion of TKE into heat.

Dimensional analysis of ε, which has units of W kg^{-1} or equivalently, m^2 s^{-3}, yields a scaling relationship of the form:

$$\varepsilon \propto \frac{U^3}{l} \tag{2}$$

where U and l are the turbulent velocity and length scales, respectively (e.g., Craig & Banner, 1994). In the absence of surface waves (i.e., the OBL is a wall-bounded layer) and buoyancy fluxes, U scales as friction velocity ($u_* = \sqrt{\frac{|\tau|}{\rho}}$; $\tau = \rho\overline{u'w'}$) and l scales as z, giving rise to the Law of the Wall (LOW):

$$\varepsilon = \frac{u_*^3}{\kappa z} \tag{3}$$

with von Kármán constant, $\kappa = 0.4$. LOW is valid under the assumption that the OBL is a "constant-flux layer", usually defined to extend to the depth at which heat and momentum fluxes are 90% of their surface values (e.g., Edson & Fairall, 1998). In convective conditions, U scales as $w_* = \sqrt[3]{B_0 h}$ (B_0 is surface buoyancy flux and h is mixed layer depth), and l scales as h, resulting in

$$\varepsilon = \frac{w_*^3}{h} = B_0 \qquad (4)$$

By convention, destabilizing fluxes (buoyancy loss from the ocean) are defined positive and stabilizing fluxes (buoyancy gain into the ocean) are defined negative. Equations 3 and 4 represent simple approximations of Equation 1 in which the production of TKE by current shear or convection is balanced by its dissipation. Early studies on the validity of Equations 3 and 4 in the OBL include Shay and Gregg (1986), Anis and Moum (1992), and Brainerd and Gregg (1993).

MOST relates nondimensionalized boundary layer variables to z/L_M, where

$$L_M = \frac{-u_*^3}{\kappa B_0} \qquad (5)$$

is the Obukhov length scale that arises from dimensional analysis of the ratio of the shear and buoyancy production terms in Equation 1. The subscript M refers to its use in MOST and helps to avoid confusion with the similarly-termed Ozmidov length scale. L_M may be conceptualized as the depth at which free convection and mechanical shear contribute equally to turbulence in the ocean (e.g., Stull, 1988), thus buoyancy forcing dominates the TKE regime where $\left|\frac{z}{L_M}\right| > 1$ (production in convective conditions, suppression in stable conditions) and wind forcing dominates where $\left|\frac{z}{L_M}\right| < 1$ (Figure 1). In MOST, scaling relationships for ε take the form of

$$\frac{\varepsilon \kappa z}{u_*^3} = f\left(\frac{z}{L_M}\right) \qquad (6)$$

where $f\left(\frac{z}{L_M}\right)$ is an empirically-derived function. For example, Wyngaard and Coté (1971) collected hot wire measurements of ε in the atmospheric boundary layer (ABL) and found equations of the form:

$$\frac{\varepsilon \kappa z}{u_*^3} = \left[A^{1/M_1} + B^{1/M_2}|z/L_M|^{1/M_3}\right]^{M_4} \qquad (7)$$

where A, B, and M_i are constants and z here is height, rather than depth. In the OBL, scaling relationships for ε are typically presented as a linear combination of Equations 3 and 4,

$$\varepsilon = A\frac{u_*^3}{\kappa z} + B B_0 \qquad (8)$$

though we note that this satisfies the form of Equation 6 when rearranged (by dividing through by $\frac{u_*^3}{\kappa z}$) into the equivalent form of

$$\frac{\varepsilon \kappa z}{u_*^3} = A + B\frac{z}{L_M} \qquad (9)$$

Equation 8 was first proposed in Lombardo and Gregg (1989) for an intermediate L_M-defined regime in which both wind stress and convection contributed significantly to turbulence production, though they found it also described measurements of turbulence fairly well across all observed conditions. In Equation 8, B_0 is restricted to positive values (turbulence producing rather than suppressing).

The representation of the OBL in MOST as a wave-free, wall-bounded layer has been challenged by decades of observational studies of turbulence generated by surface wave breaking (Agrawal et al., 1992; Anis & Moum, 1995; Craig & Banner, 1994; Drennan et al., 1992; Gemmrich & Farmer, 2004; Soloviev & Lukas, 2003; Terray et al., 1996) and wind-wave interaction (D'Asaro, 2014; Sutherland et al., 2014). Wave breaking directly injects turbulence into the near-surface "breaking layer", which extends down to a depth of approximately 0.6 times the significant wave height (H_s) (Gerbi et al., 2009; Terray et al., 1996). TKE generated in this layer
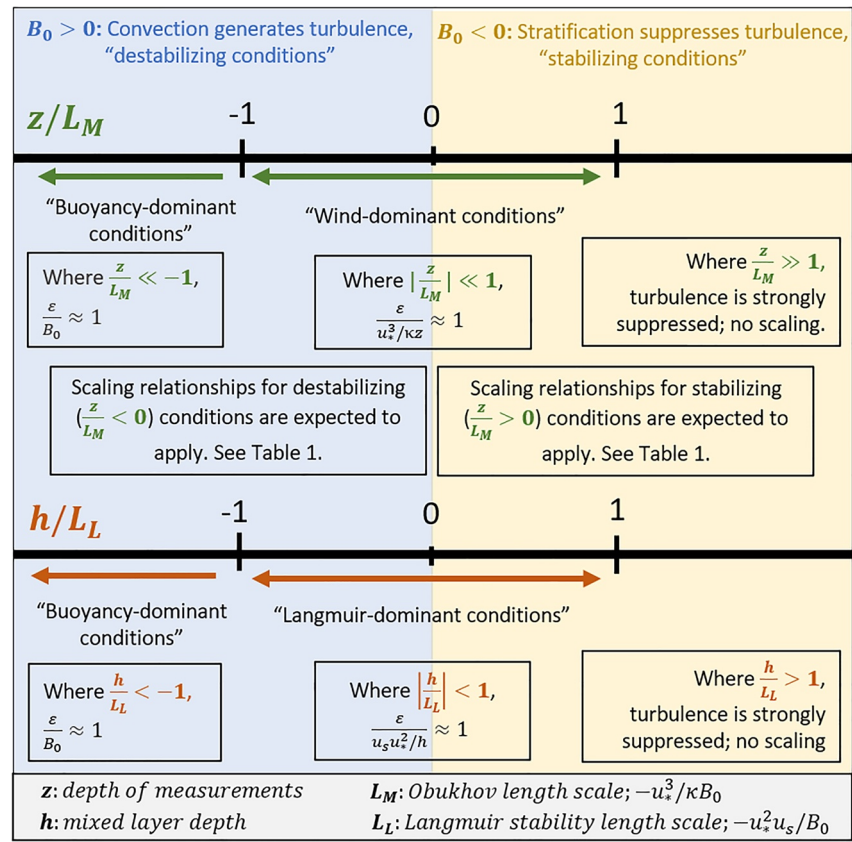
Figure 1. Visual representation of the definitions for destabilizing and stabilizing conditions and turbulence dominance regimes, as defined using the Obukhov length scale (L_M; Equation 5) and the Langmuir stability length scale (L_L; Equation 11). Also shown are where scaling relationships of the form of Equation 2 are expected to apply.

is transported downwards to a "transition layer", also known as wave-affected surface layer (WASL) (Gerbi et al., 2009; Stips et al., 2005). According to Terray et al. (1996), this transition layer is bounded below by the transition depth, $z_t = 0.3\kappa \bar{c}/u_*$, where $\bar{c}$ is an effective phase speed related to the flux of energy from wind stress into the wave field. Though observational studies have since shown mixed results on the presence or extent of the transition layer as defined by Terray et al. (1996) (Esters et al., 2018; Sutherland & Melville, 2015), it is well established that wave breaking causes ε to deviate from LOW and B_0 scalings in the near-surface.

While TKE generated through surface wave breaking and the shear of Stokes drift velocities is largely confined to the upper few meters of the water column, Langmuir circulation can distribute turbulence to the base of the mixed layer through its associated enhancement of vertical transport. Because of its importance to mixed layer deepening, there have been many efforts to parameterize the influence of Langmuir circulation in models of the OBL (Li et al., 2019). The Langmuir number,

$$La = \sqrt{u_*/u_s} \tag{10}$$

arises from a scaled ratio of the shear and Stokes production terms in Equation 1 and describes the strength of Langmuir circulation (McWilliams et al., 1997). For well-developed seas, La is typically ~ 0.4 (Belcher et al., 2012; Sutherland et al., 2014), though misalignment of wind and waves is known to broaden the range of La (Van Roekel et al., 2012). According to large eddy simulation (LES) results from Grant and Belcher (2009), a distinct Langmuir-driven regime is defined where $La < 0.5$, with the transition to a wind-dominant regime occurring between $0.5 < La < 2$. A second term, the Langmuir stability length scale,

$$L_L = -\frac{u_s u_*^2}{B_0} \tag{11}$$

similarly arises from the scaled ratio of the Stokes production and buoyancy terms in Equation 1 and serves as an analog to L_M, which is a scaled ratio of the shear production and buoyancy terms. Just as $\frac{z}{L_M}$ is used to delineate wind-dominant and buoyancy-dominant turbulence regimes, $\frac{h}{L_L}$ defines Langmuir-dominant $\left(\left|\frac{h}{L_L}\right| < 1\right)$ and buoyancy-dominant $\left(\left|\frac{h}{L_L}\right| > 1\right)$ regimes (Belcher et al., 2012, Figure 1). As L_L contains both u_s and u_*, it is sometimes also used to delineate a buoyancy-dominant regime and that of a composite "wind-wave-induced" turbulence that includes the contributions of both shear and Stokes production (Esters et al., 2018; Sutherland et al., 2014).

Because wind and waves are intrinsically tied, there is some question as to whether it is necessary to parameterize Langmuir circulation separately, or if the implicit incorporation of wave effects in traditional wind-based parameterizations is sufficient. In their model study on the global prevalence of Langmuir circulation, Belcher et al. (2012) argued for the former, reasoning that wind and waves are rarely in equilibrium and citing variability in the ratio of u_s to u_* as evidenced by the large range in their computed values of La across the world's oceans. Conversely, a number of observational studies have found u_s to scale linearly with u_* (Esters et al., 2018; Gargett & Grosch, 2014; Kitaigorodskii et al., 1983). In cases where u_s is linearly proportional to u_*, it follows that that La is relatively constant and thus L_L and L_M become linearly proportional as well, as $L_M = \frac{1}{\kappa} La^2 L_L$.

Belcher et al. (2012) presented a framework based on La and L_L that has been used by both observational (Esters et al., 2018) and LES studies (Li et al., 2019; Li & Fox-Kemper, 2017) to assess the relative contributions of wind-driven current shear, buoyancy flux, and Langmuir circulation to the overall turbulence regime. This framework defines TKE as a linear combination of the three forcings, similarly to Equation 8:

$$\varepsilon\left(\frac{z}{h} = 0.5\right) = A_s \frac{u_*^3}{h} + A_L \frac{w_{*L}^3}{h} + A_c \frac{w_*^3}{h} \tag{12}$$

where $w_{*L} = \left(u_s u_*^2\right)^{1/3}$ is the velocity scale for Langmuir turbulence and $A_s = 2\left(1 - e^{-\frac{1}{2}L_a}\right)$, $A_L = 0.22$, and $A_c = 0.3$ are coefficients derived from LES studies. Equation 12 applies where z is half of h, an arbitrary depth chosen to discern where the three forcings are well established. A_s is made a function of L_a to account for the inhibition of vertical velocity shear, and thus shear production, by the enhanced vertical velocities associated with Langmuir circulation. Equation 12 is rearranged into a scaling relationship of the form

$$\frac{\varepsilon\left(\frac{z}{h} = 0.5\right)}{\frac{u_*^3}{h}} = A_s + A_L La^{-2} + A_c La^{-2} \frac{h}{L_L} \; where \; B_0 > 0 \tag{13}$$

which is used to define a turbulence regime diagram in $La - h/L_L$ space (e.g., Figure 3). The three "corners" of this diagram denote regimes where either wind, Langmuir, or buoyancy is the dominant forcing.

3. Data and Methods

3.1. Pulse-Coherent ADCP

Fine-scale velocity measurements were collected with a 2 MHz Nortek AquaDopp High-Resolution (HR) velocity profiler installed at 8.4 m water depth on the mooring line and outfitted with a fin that allowed it to remain in-line with and facing the prevailing current (see Zippel et al., 2021). The AquaDopp HR is a pulse-coherent ADCP that transmits two sequential pulses of which the phase shift allows for the calculation of radial velocities at centimeter-scale resolution. The specifics and validation of obtaining microstructure turbulence measurements using pulse-coherent ADCPs were first described in Veron and Melville (1999) and later in the context of moored deployments in Zippel et al. (2021). The instrument was fitted with a custom sensor head with 3 beams: two beams in a plane orthogonal to the cylindrical axis and a third beam directed upward 45° to this plane and 45° between the two horizontal orthogonal beams. The system was set to sample only Beam 1, one of the two horizontal beams orthogonal to the instrument axis and the one facing into the flow along the axis of the vane, in order to maximize the sample rate at 4 Hz. Profiles of along-beam velocities were 1.38 m total in length and range-gated into 53 cells, each 26 mm in size. The nominal velocity range in each bin was ±10.5 cm s⁻¹ and

sampling occurred over 135 s "bursts" once every hour at a rate of 4 Hz for a total of 540 profiles per burst. Over 5,000 bursts were collected in total over the 9-month study period beginning in October 2008 and ending in July 2009.

3.2. Calculation of TKE Dissipation Rate

The AquaDopp HR appeared significantly bio-fouled upon recovery, so velocity measurements were truncated at 02-July-2009, shortly before the velocity and corresponding ping correlation values (a measure of strength-of-return) became erratic. The remaining data were quality-controlled and used to calculate ϵ following the methods detailed in Zippel et al. (2021). A simplified overview of these methods is provided here.

Data are first corrected for phase wrapping, an artifact associated with pulse-coherent ADCPs in which radial velocities exceeding a so-called ambiguity velocity "wrap around" and are recorded as abruptly high or low values in multiples of 2π. Then, "unwrapped" velocity profiles with an averaged ping correlation lower than 60% and individual pings with correlations lower than 40% are removed. Power spectra are calculated from the 540 individual velocity profiles collected during each 135 s burst, then averaged together into a single, burst-averaged power spectrum. ϵ is estimated from the inertial subrange of each burst-averaged spectrum, defined as the region where the slope of the spectrum is equal to the theoretical $-5/3$ from Kolmogorov's "5/3 law" for energy distribution in a turbulent fluid (Kolmogorov, 1941):

$$E(k) = C_1 \epsilon^{2/3} k^{-5/3} \tag{14}$$

Here, $E(k)$ is the power spectral density of turbulent velocities in the inertial subrange, k is wavenumber, and $C_1 = 0.53$ (Sreenivasan, 1995). In practice, we obtain ϵ by performing a least square regression on a spectrum of the form:

$$E(k) = G(k, L_T, L_R)(C_1 \epsilon^{2/3} k^{-5/3} + N) \tag{15}$$

where $G(k, L_T, L_R)$ (Zippel et al., 2021; Equation 13 therein) is an instrument transfer function that accounts for the spatial sampling filter arising from the near-rectangular sampling windows of the instrument's transmit and receive pulses, of lengths L_T and L_R, respectively, and N is instrument noise. By solving separately for N, the amount of noise affecting the solution for ϵ is reduced.

However, some noise in the estimation of ϵ is inevitable, so we estimate confidence intervals for each estimate of ϵ as

$$\epsilon \pm t_{95\%} SE_\epsilon \tag{16}$$

where t is the critical t-value for a 95% confidence level for a given number of degrees of freedom (the number of wavenumbers bins across which the inertial subrange is evaluated) and SE_ϵ is the standard error of the regression solution for ϵ. Quantile-quantile plots of the regression residuals suggest sufficiently normal distributions for Equation 16 to apply. Measurements of ϵ below 10^{-9} W kg^{-1} (constituting 3% of total data) are masked as they are very likely below the ping correlation-dependent instrument noise floor, as reported for a similar pulse-coherent ADCP configuration in Zippel et al. (2021).

3.3. Temperature, Salinity, and Mixed Layer Depth

Temperature and salinity were measured from a suite of conductivity-temperature loggers installed on the mooring line at depths of 0.90, 3.7, 6.8, 16, 30, 38, 40, 63, 85, 96, 130, 160, 190, 220, 250, and 310 m. Four different sensor models were used: RBR XR-420, Sea-Bird Electronics (SBE)-39, SBE-16, and SBE-37. Mixed layer depth, h, was calculated using hourly-averaged temperature measurements interpolated over half meter intervals, and defined to extend down to the depth at which temperature first differs by 0.1° from the surface.

3.4. Meteorological Measurements

Wind speed, wind direction, air temperature, humidity, shortwave radiation, and longwave radiation were recorded once per minute from an Improved Meteorological (IMET) sensor suite installed on the buoy about 2.7 m above sea surface (Colbo & Weller, 2009). Surface buoyancy flux, defined positive out of the ocean and in units of Wkg^{-1}, was calculated as

$$B_0 = -\frac{g\alpha Q_{net}}{\rho c_p} + g\beta(E - P)S_0 \tag{17}$$

where g is gravity, α is the thermal expansion coefficient, Q_{net} is surface heat flux, ρ is ocean density, c_p is the specific heat of water, β is the haline contraction coefficient, E and P are the rates of evaporation and precipitation, and S_0 is the surface salinity. P, measured using a rain gauge on the buoy, was effectively $0\,ms^{-1}$ across the entire study period. Q_{net} is calculated as the net sum of the shortwave, net longwave, latent, and sensible fluxes, with net longwave radiation and the turbulent heat fluxes calculated using version 3.6 of the COARE bulk flux algorithm (Fairall et al., 1996, 2003). Only the amount of shortwave radiation absorbed in the mixed layer (I) is used in the calculation of Q_{net}, which can at times exclude upwards of 20% of the total incoming radiation (I_0). This is calculated as:

$$I = I_0 - \left[I_0\left(I_1 e^{-\frac{h}{\lambda_1}} + I_2 e^{-\frac{h}{\lambda_2}}\right)\right] \tag{18}$$

where subscripts 1 and 2 indicate the shortwave and longwave components of insolation, following Price et al. (1986). $I_1 = 0.62$, $I_2 = 1 - 0.62$, $\lambda_1 = 0.6\,m$, $\lambda_2 = 20\,m$ for fairly clear, mid-ocean water (Paulson & Simpson, 1977). COARE was also used to calculate E and wind stress ($\tau = \rho\overline{u'w'}$). Water-side friction velocity was calculated as $u_* = \left(\frac{|\tau|}{\rho}\right)^{\frac{1}{2}}$ and, c_p, β and ρ were calculated with the Gibbs-SeaWater Oceanographic Toolbox (McDougall & Barker, 2011). Meteorological variables used in analyses were averaged across the hour.

3.5. Wave Measurements

Hourly wave spectra were acquired using the National Buoy Data Center (NBDC) wave and marine data acquisition system (WAMDAS; Teng et al., 2005) installed on the mooring's 2.7 m-diameter surface buoy. The inertial measurement unit for the WAMDAS was installed inside the buoy, near the water line. Two-dimensional wave frequency spectra were calculated from the wave spectral density and Longuet-Higgins Fourier Coefficients provided for the Stratus mooring station by the NBDC. The measured frequencies ranged from 0.020 to 0.485 Hz and higher frequencies were estimated using an f^{-5} spectral tail calculated according to Appendix B of Webb and Fox-Kemper (2015). Though patching on an f^{-5} tail is a standard method of extending the spectra beyond what is feasibly measured, we recognize that it may result in an underestimation of Stokes drift on the order of $\sim$10–30% if the highest measured ("cut-off") frequency is lower than that of the transition between equilibrium and saturation ranges (Lenain & Pizzo, 2020). Stokes drift at the surface is calculated as

$$u_s|_{z=0} \approx \frac{16\pi^3}{g}\int_0^\infty \int_{-\pi}^{\pi}(\cos\theta, \sin\theta, 0)f^3 S_{f\theta}(f, \theta)d\theta df \tag{19}$$

where f is frequency and $S_{f\theta}$ is the directional wave spectrum. To obtain the component of the Stokes drift in the direction of the wind, Equation 19 is multiplied by the cosine of the difference between the direction of Stokes drift with that of the wind. From here onward, u_s denotes the component of the surface Stokes drift in the direction of the wind.

The wind-sea separation frequency was calculated systematically using methods described in Wang and Hwang (2001) and Hwang et al. (2011). Significant wave height of the wind-sea, H_{sw}, is defined as $4\sqrt{m_0}$, where m_0 is the integral (zeroth moment) of the 1-D wave spectral density of the wind-sea spectra. Phase speed is calculated as $c_p = 1.56/f_{peak}$, where f_{peak} is the peak frequency of the wind-sea. The wave transition depth,

$z_t = 0.3\kappa\bar{c}/u_*$, was calculated using the approximation $\bar{c} = \frac{1}{2}c_p$, which Terray et al. (1996) shows to represent an upper-bound estimate.

3.6. Removal of Data Near the Top and Bottom Boundaries of the Mixed Layer

The MOST and Belcher et al. (2012) frameworks are applicable to turbulence generated by wind-driven current shear, buoyancy flux, and in the case of the latter, Langmuir circulation, and are valid within the mixed layer, which is assumed to approximate a constant flux layer. We therefore seek to remove data influenced by extraneous processes such as surface or internal wave breaking, as well as data collected during periods in which the mixed layer was shallower than the depth of the instrument.

As discussed in Section 2, surface wave breaking is a common cause for measurements of ϵ to deviate from MOST. While the depth of our instrument at 8.4 m is consistently 3–4 times that of H_{sw} (Figure 2d) and therefore out of the direct influence of breaking wave turbulence, calculation of z_t from Terray et al. (1996) suggests that up to 10% of our data may fall within the transition layer. Average values of z_t were 5.5 m and ranged as deep as 13.6 m. Because z_t does not always clearly delineate scaling regimes in observational data (Esters et al., 2018) and because our calculation of $\bar{c}$ likely results in an overestimation of z_t, as described in Section 3.5, we choose not to address the potential influence of surface wave breaking by simply removing data corresponding to z_t greater than the depth of the instrument. Instead, we examine measurements of ϵ scaled according to Equation 2, where U is equal to u_*, w_*, and w_{*L}, as a function of $\frac{z}{h}$ in Figure S1 in Supporting Information S1. There is a marked deviation in the binned-median profiles of scaled ϵ where $\frac{z}{h} < 0.135$ that suggests an extraneous source of turbulence at the depth of the instrument coinciding with the deepest values of h. We speculate that when h is at its deepest, the transition zone is also at its deepest and most likely to encompass our instrument, causing measured ϵ to deviate from Equation 2. The correspondence of $z_t > z$ (Figure S1 in Supporting Information S1; blue data points) with deeper mixed layer depths ($\frac{z}{h} \ll 1$) supports a link between the depths of the transition layer and mixed layer. We
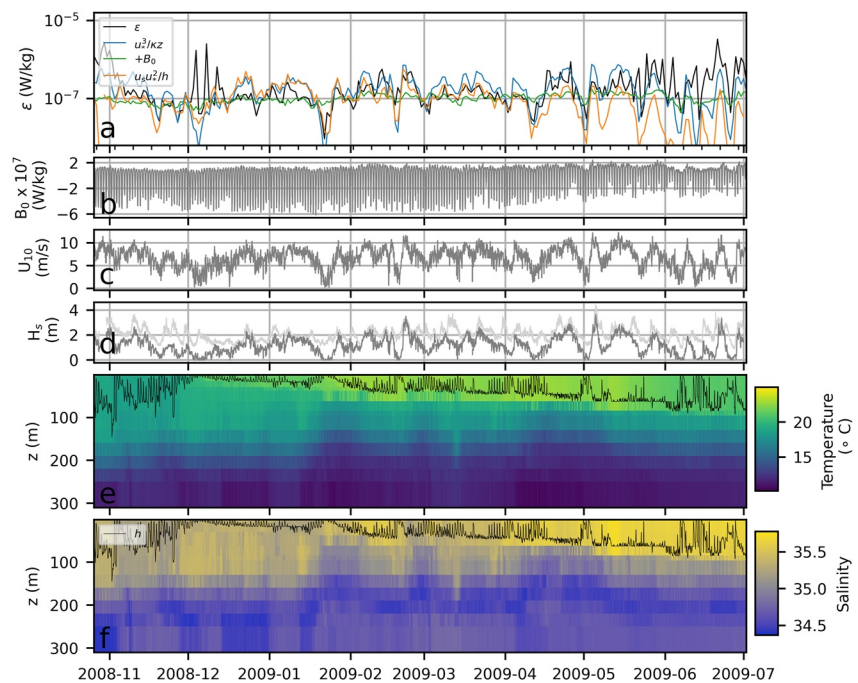

Figure 2. Time series of (a) TKE dissipation rate (ϵ) overlaid with $u_*^3/\kappa z$, destabilizing (positive) surface buoyancy flux ($+B_0$), and $u_s u_*^2/h$, (b) surface buoyancy flux (B_0), (c) wind speeds at 10 m height (U_{10}), (d) significant wave height (H_s) calculated from measured wave spectra (full spectrum in light gray, wind-sea in dark gray), (e) potential temperature and (f) practical salinity, overlaid by mixed layer depth (h; black line). ϵ is shown in as a daily average for visual clarity while the remaining variables are shown at a 1-hr frequency.
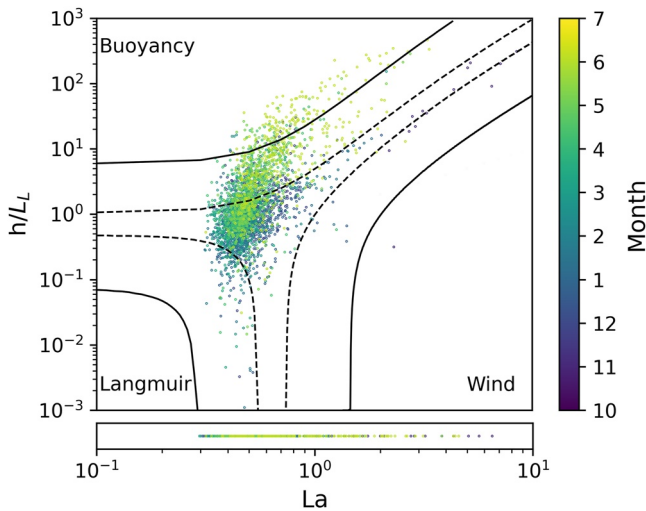
Figure 3. Turbulence regime diagram showing the relative contributions to TKE by destabilizing buoyancy fluxes, Langmuir circulation, and wind-generated current shear, after Belcher et al. (2012). Data are colored by the calendar month during which they were collected, with partial data from July and October and no data from August and September. Solid and dashed lines indicate regions where 90% and 60%, respectively, of overall TKE is generated by a single forcing, as calculated from Equation 13. The regime diagram is defined only for destabilizing buoyancy fluxes, so data in stabilizing conditions are shown in 1-dimensional L_a space below.

therefore remove data where $\frac{z}{h} < 0.135$ as a heuristic means of minimizing the probable influence of surface wave breaking (Figure S1 in Supporting Information S1; lower shaded region).

In addition, data collected during periods when the instrument resided below ($\frac{z}{h} > 1$) or very near to the base of the mixed layer ($\frac{z}{h} \sim 1$) should be removed. We remove data where $\frac{z}{h} > 0.5$ (Figure S2 in Supporting Information S1; upper shaded region), a threshold slightly more conservative than $z = h$. This was done for two reasons, (a) proximity to the interface between the mixed layer and the pycnocline below can expose the instrument to TKE generated by processes such as internal wave breaking and inertial shear and (b) the spacing of temperature measurements near the ADCP, at 6.8 and 16.0 m, lends some uncertainty to the precision of $z = h$.

In summary, only measurements of ε within the range of $0.135 < \frac{z}{h} < 0.5$ are considered in the analyses described in Section 4 below. This excludes ~30% of measurements in destabilizing conditions and ~60% in stabilizing conditions.

4. Results

4.1. Conditions at the Stratus Mooring Site

Figure 2 shows the time series measurements of ε (Figure 2a), B_0 (Figure 2b), 10 m wind speed (U_{10}; Figure 2c), significant wave heights (Figure 2d), temperature (Figure 2e), and salinity (Figure 2f). ε is shown as a daily average for visual clarity while the remaining variables are shown at a 1-hr resolution. The average hourly standard deviation of the wind direction is 7.4°, consist-

ent with the directionally steady trade wind regime noted by Weller (2015). The magnitude of wind forcing is also fairly steady across the study period, with an average $U_{10} = 6.7 \, \text{m s}^{-1}$, standard deviation of $2.2 \, \text{m s}^{-1}$, and average hourly change of $0.64 \, \text{m s}^{-1}$ (Figure 2c). However, there are several days-long periods where wind speeds drop to near-zero across the study period, such as in late January and mid-May. Trade winds in the region are driven by a high-pressure cell to the southwest of the mooring, and dip when this cell is shifted and its associated pressure gradient is weakened (Weller et al., 2014). Dissipation rate drops in response to these dips in wind speed, though the magnitude of this response is variable (Figure 2a).

Wave spectra (not shown) indicate that the wind-sea propagates primarily to the northwest whereas swell, originating from storms in the South Pacific, is primarily to the northeast. The equilibrium state of wind and wind-sea can be inferred with wave age, $\frac{c_p}{U_{10}}$, with young seas where $\frac{c_p}{U_{10}} < 0.8$, mature seas where $0.8 < \frac{c_p}{U_{10}} < 2$, and old seas where $\frac{c_p}{U_{10}} > 2$ (Edson et al., 2007). The average wave age of the wind-sea for conditions of $U_{10} > 3 \, \text{m s}^{-1}$ is 1.8 with a standard deviation of 1, suggesting the prevalence of mature seas at the mooring site. There is a clear linear dependence between u_s and u_*, with $u_s = 5.5u_* + 9 \times 10^{-3}$ and an r^2 value of 0.62 (Figure S2 in Supporting Information S1). From November through May, La is fairly constant with an average of 0.51 and a standard deviation of 0.16. In June, the average and standard deviation are higher, at 0.86 and 0.72, respectively.

Temperature and salinity data show the presence of the cold, fresh (11–13°C, 34.1–34.3; Schneider et al., 2003) Eastern South Pacific Intermediate Water (ESPIW) underlying the mixed layer at about ~200 m (Figures 2e and 2f). The mixed layer depth, h, deepens throughout austral fall and into winter, broadly tracking an increase in destabilizing buoyancy fluxes (Figure 2b). h responds to wind speed (Figure 2c) on shorter timescales, such as in late January when wind speeds drop to near $0 \, \text{m s}^{-1}$ and h abruptly shoals.

Figure 2a is overlain with daily-averages of Equation 2, with $U = u_*$, w_* and w_{*L}: $\frac{u_*^3}{\kappa z}$, (positive) B_0, and $\frac{u_s u_*^2}{h}$. There are periods of time, such as late February, where $\frac{u_*^3}{\kappa z}$ and $\frac{u_s u_*^2}{h}$ capture the magnitude of daily-averaged ε well, and other periods of time, such as in late December, where B_0 appears to perform better, though its small dynamical range perhaps limits its overall predictive power. There are also periods where the Langmuir scaling matches
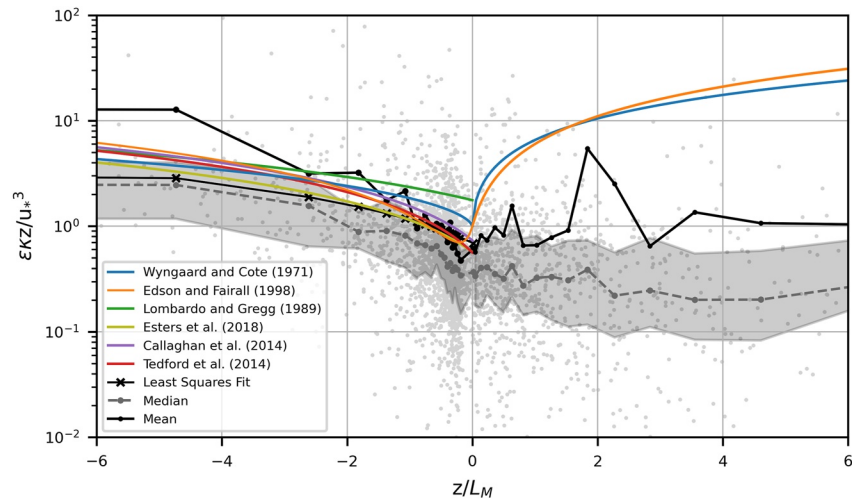
Figure 4. Measurements of ε (away from the top and bottom of the mixed layer; $\mathbf{0.135 < \frac{z}{h} < 0.5}$) scaled by $u_*^3/\kappa z$ across z/L_M regimes. Negative z/L_M corresponds to destabilizing conditions. The mean and median of bins containing equal numbers of data are denoted by the dashed gray and solid black lines, respectively. The shaded region indicates the interquartile range. The overlaid scaling relationships are defined in Table 1 and the least squares fit by Equation 20.

the magnitude of ε more closely than $\frac{u_*^3}{\kappa z}$ (all of March), and vice versa (late May). This is indicative of differing turbulence regimes at the mooring site, which are examined further in Section 4.4. Figure 3 shows the Belcher et al. (2012) turbulence regime diagram defined by Equation 13, which suggests the relative contributions of destabilizing surface buoyancy flux, wind-driven current shear, and Langmuir processes to turbulence at this site. Calculated values of scaled ε are colored by month to highlight variability in the dominant turbulence regime across seasons. Stabilizing buoyancy flux conditions are represented in 1-dimensional La space below. As in Belcher et al. (2012) and following Leibovich (1983), La is calculated only for values of U_{10} above 3 m/s, which excludes 3% of data in conditions of destabilizing B_0 and 8% in conditions of stabilizing B_0. The black lines indicate regions where a single forcing is the dominant mechanism of turbulence production (i.e., "wind-dominant", "buoyancy-dominant", or "Langmuir-dominant"); the dotted and solid lines nominally indicate a 60% and 90% contribution, respectively, to overall turbulence, as calculated from ratios of the terms in Equation 13. Turbulence appears more buoyancy-forced in early austral winter months (yellow) than during the rest of the study period, when a mix of buoyant- and Langmuir-forced conditions prevail.

4.2. Scaling of ε Across z/L_M

We first examine the scaling of ε measurements in Figure 4, where individual values of ε scaled by $\frac{u_*^3}{\kappa z}$ are shown across the full range of z/L_M in both stabilizing ($\frac{z}{L_M} > 0$) and destabilizing ($\frac{z}{L_M} < 0$) conditions. Overlaid on the individual data points are the mean, median, and interquartile range computed on values of $\frac{\varepsilon \kappa z}{u_*^3}$ grouped in $\frac{z}{L_M}$ bins containing equal numbers of data points. Also shown overlaid are scaling relationships developed in prior studies of the ABL (Edson & Fairall, 1998; Wyngaard & Coté, 1971), OBL (Callaghan et al., 2014; Esters et al., 2018; Lombardo & Gregg, 1989), and lake surface boundary layer (Tedford et al., 2014). The scaling relationships, detailed in Table 1, are evaluated at each bin across the full $\frac{z}{L_M}$ range of our data, though the actual ranges of conditions from which they were developed were either narrower or unspecified. We note that the scaling relationship from Esters et al. (2018) is defined for conditions of buoyancy dominance, $\frac{h_\varepsilon}{L_L} > 1$, where h_ε is the active mixing layer, though we present it across all data where $B_0 > 0$.

In destabilizing conditions, all of the previously published scaling relationships except for those of Wyngaard and Coté (1971) and Lombardo and Gregg (1989) align with the binned means of our data roughly where $\frac{z}{L_M} > -1$. Where $-3 < \frac{z}{L_M} < -1$, the scaling relationships of Wyngaard and Coté (1971) and Lombardo and Gregg (1989) align better than the rest, and where $\frac{z}{L_M} < -3$, all scaling relationships diverge from the binned means of our data. In stabilizing conditions, the binned means of our data vary mostly about unity with little apparent depend-

Table 1
Scaling Relationships Examined in Figure 4

Study	Setting	Instrumentation	Scaling relationship for ε
Wyngaard and Coté (1971)	ABL; Wheat field	Hot-wire anemometer	$\frac{\varepsilon \kappa z}{u_*^3} = \left[1 + 0.5\left\|\frac{z}{L}\right\|^{2/3}\right]^{3/2}$ where $\frac{z}{L_M} < 0$
			$\frac{\varepsilon \kappa z}{u_*^3} = \left[1 + 2.5\left(\frac{z}{L}\right)^{3/5}\right]^{3/2}$ where $\frac{z}{L_M} > 0$
Edson and Fairall (1998)	Marine ABL; Northeast Pacific, Northwest Atlantic	Sonic anemometer	$\frac{\varepsilon \kappa z}{u_*^3} = \frac{1 - \frac{z}{L_M}}{1 - 7\frac{z}{L_M}} - \frac{z}{L_M}$ where $\frac{z}{L_M} < 0$
			$\frac{\varepsilon \kappa z}{u_*^3} = 1 + 5\frac{z}{L_M}$ where $\frac{z}{L_M} > 0$
Lombardo and Gregg (1989)	Northeast Pacific	Descending microstructure profiler	$\varepsilon = 1.76\frac{u_*^3}{\kappa z} + 0.58 B_0$ where $\frac{h}{L_M} > 0$
Esters et al. (2018)	Subtropical and North Atlantic, Arctic Ocean	Ascending microstructure profiler	$\varepsilon = 0.63\left(0.90\frac{u_*^3}{\kappa z} + 0.91 B_0\right)$ where $\frac{h_\varepsilon}{L_L} > 1$
Callaghan et al. (2014)	Indian Ocean	Ascending microstructure profiler	$\varepsilon = 0.73\frac{u_*^3}{\kappa z} + 0.81 B_0$ where $B_0 > 0$
Tedford et al. (2014)	Lake Pleasant, New York	Ascending temperature-gradient microstructure profiler	$\varepsilon = 0.56\frac{u_*^3}{\kappa z} + 0.77 B_0$ where $B_0 > 0$

Note. The relationships are written as they are presented in the original literature; z is defined positive upward in the ABL as well as positive downward in the OBL.

ence on $\frac{z}{L_M}$ and are poorly described by the scaling relationships of Wyngaard and Coté (1971) and Edson and Fairall (1998).

We define our own scaling relationship for destabilizing conditions by performing a least squares regression of $\frac{\varepsilon \kappa z}{u_*^3}$ and $\frac{z}{L_M}$ to the form of Equation 9, excluding the highest and lowest 1% of $\frac{\varepsilon \kappa z}{u_*^3}$ values:

$$\frac{\varepsilon \kappa z}{u_*^3} = 0.69 - \frac{0.46z}{L_M}, \tag{20}$$

Equation 20 is shown in Figure 4 computed with binned values of z/L_M. The equivalent dimensional form is:

$$\varepsilon = 0.69\frac{u_*^3}{\kappa z} - 0.46 B_0 \tag{21}$$

4.3. Scaling of ε in Distinct Turbulence Regimes

The three major sources of turbulence considered here are wind-driven current shear, destabilizing surface buoyancy flux, and Langmuir turbulence, which have velocity and length scales of u_* and z, w_* and h, and w_{*L} and h, respectively. The associated variations of Equation 2 ($\frac{u_*^3}{\kappa z}$, B_0, and $\frac{u_s u_*^2}{h}$) are expected to be approximately equal to ε when their respective sources of turbulence dominate the overall turbulence regime. These dominance regimes, henceforth referred to as "wind-dominant", "buoyancy-dominant", and "Langmuir-dominant" regimes, are delineated using $\frac{z}{L_M}$ or $\frac{h}{L_L}$ (see Section 2 and Figure 1). Measurements of ε should scale to $\frac{u_*^3}{\kappa z}$ where $\left|\frac{z}{L_M}\right| \ll 1$ and to B_0 where $\frac{z}{L_M} \ll -1$; In order to satisfy these definitions while retaining a sufficient number of data points, we define the cutoff for the MOST wind-dominant regime as $\left|\frac{z}{L_M}\right| < 0.3$ and for the buoyancy-dominant regime as $\frac{z}{L_M} < -3$. We similarly define cutoffs of $\left|\frac{h}{L_L}\right| < 0.5$ for the Belcher framework wind- and Langmuir-dominant regimes and $\frac{h}{L_L} > 5$ for the buoyancy-dominant regime.

It is standard to assess scalings of the form of Equation 2 based on how closely the average value of scaled ε falls to unity (e.g., Lombardo & Gregg, 1989). Summary statistics of ε scaled by $\frac{u_*^3}{\kappa z}$, B_0, and $\frac{u_s u_*^2}{h}$ in destabilizing conditions are presented in Table 2 and by $\frac{u_*^3}{\kappa z}$ and $\frac{u_s u_*^2}{h}$ in stabilizing conditions in Table 3. Statistics are bolded for each scaling in their respective dominance regimes, where they are expected to apply. Though the mean is the standard descriptor in studies of turbulence, we additionally report the median and interquartile range to provide additional insight on the spread of the data. Because ε is approximately log-normally distributed, the mean is

Table 2

Median, Mean, and Interquartile Range (Q75-Q25) of ε Scaled by $\frac{u_*^3}{\kappa z}$, B_0, and $\frac{u_s u_*^2}{h}$ in Destabilizing Conditions ($B_0 > 0$)

Destabilizing conditions	All	$\frac{h}{L_L} > -0.5$ (Langmuir-dominant)	$\frac{z}{L_M} > -0.3$ (wind- dominant)	$\frac{h}{L_L} < -5$ (B_0 - dominant)	$\frac{z}{L_M} < -3$ (B_0 -dominant)
n	2,226	400	517	368	149
$\varepsilon z\kappa/u_*^3$					
Median	0.56	**0.40**	**0.38**	1.36	2.86
Mean	2.45	**0.67**	**0.60**	10.04	20.90
Q75–Q25	1.13	**0.50**	**0.48**	2.77	6.55
ε / B_0					
Median	1.05	1.52	1.60	**0.63**	**0.61**
Mean	2.79	3.31	3.87	**2.87**	**2.49**
Q75–Q25	1.96	2.04	2.31	**1.16**	**0.86**
$\varepsilon h/u_s u_*^2$					
Median	1.32	**0.56**	0.83	8.10	12.11
Mean	21.20	**1.03**	6.48	123.75	243.37
Q75–Q25	3.27	**0.62**	1.27	20.91	42.50

Note. Only data away from the top and bottom of the mixed layer ($0.135 < \frac{z}{h} < 0.5$) are considered. Statistics are bolded for each scaling in their respective dominance regimes, where they are expected to apply.

always higher than the median. The average of $\frac{\varepsilon\kappa z}{u_*^3}$ is ~0.65 across both destabilizing and stabilizing conditions in the Langmuir- and wind-dominant regimes. This slight deviation from unity is typical in observational studies and discussed further in Section 5. The Langmuir scaling is less consistent, scaling ε to averages of 1.03 in destabilizing conditions and 1.55 in stabilizing conditions. B_0 is only applicable to destabilizing conditions, where it scales ε to averages of 2.9 and 2.5. Notably, the mean and median of $\frac{\varepsilon}{B_0}$ are roughly a factor 5 apart (Table 2), suggesting that the influence of outliers in which B_0 underestimates measured ε is strong.

The interquartile range, which contains 50% of all data and describes their spread about the median, is reduced for each scaling in its dominant regime relative to the entire dataset, and increased in non-dominant regimes. For example, the interquartile range of ε scaled by $\frac{u_*^3}{\kappa z}$ in Table 2 is decreased from ~1.1 across all destabilizing conditions to ~0.5 in the wind-dominant regimes, but increased to upwards of 2 in the buoyancy-dominant regimes. That the spread of ε scaled by $\frac{u_*^3}{\kappa z}$, B_0, and $\frac{u_s u_*^2}{h}$ is reduced in the regimes where each scaling is expected to apply, and increased where they are not, lends confidence to the ability of the scalings to collapse measurements of ε close to unity.

We examine the scaling of ε by $\frac{u_*^3}{\kappa z}$, B_0, and $\frac{u_s u_*^2}{h}$ in destabilizing conditions in greater detail by plotting individual measurements of ε directly against calculated values of each scaling. This is shown in Figure 5 with dominance regimes defined by $\frac{z}{L_M}$, and by $\frac{h}{L_L}$ in Figure 6. The medians and means binned across the x-axis are shown as blue and orange markers, respectively. Binned medians and means are also computed with the upper and lower confidence bounds of the 95% confidence interval of ε (Equation 16) and shown as shaded blue and orange regions. A 1:1 line is shown in each panel to represent idealized conditions where the scaling and measured ε are equivalent. In Figures 5 and 6, all panels show some, if not most, binned means deviating from this 1:1 line, reflecting the less-than-unity means in Table 2. Also shown in Figures 5a and 5b is Equation 21 calculated using bin-averaged values of $\frac{u_*^3}{\kappa z}$ and B_0. MOST attempts to reflect the varying contributions of surface buoyancy fluxes and wind-driven current shear across a range of $\frac{z}{L_M}$ and therefore should represent realistic conditions better than the 1:1 line,
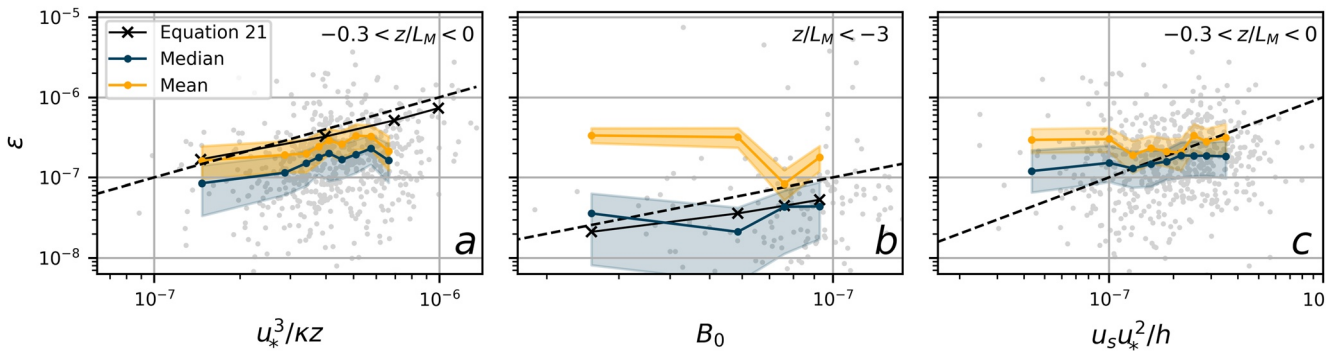
Table 3

Same as in Table 2, but in Stabilizing Conditions ($B_0 < 0$)

Stabilizing conditions	All	$\frac{h}{L_L} < 0.5$ (Langmuir-dominant)	$\frac{z}{L_M} < 0.3$ (Wind-dominant)	$\frac{h}{L_L} > 5$ (B_0 dominant)	$\frac{z}{L_M} > 3$ (B_0 dominant)
n	1064	175	177	318	247
$\varepsilon z\kappa/u_*^3$					
Median	0.34	**0.35**	**0.37**	0.38	0.35
Mean	3.41	**0.61**	**0.69**	9.55	11.78
Q75–Q25	0.78	**0.49**	**0.51**	0.86	0.97
$\varepsilon h/u_s u_*^2$					
Median	0.77	**0.64**	0.84	1.10	0.79
Mean	34.89	**1.55**	2.37	115.65	130.78
Q75–Q25	1.72	**0.76**	1.16	4.86	3.48

Figure 5. Measurements of ε (away from the top and bottom of the mixed layer; $\mathbf{0.135 < \frac{z}{h} < 0.5}$) in destabilizing conditions plotted directly against $\frac{u_*^3}{\kappa z}$, $\mathbf{B_0}$, and $\frac{u_s u_*^2}{h}$. Dominant forcing regimes are defined using $\frac{z}{L_M}$, with $\frac{z}{L_M} < -0.3$ denoting a buoyancy-dominant regime and $\frac{z}{L_M} > -3$ denoting a shear-dominant regime. The dashed black line is a 1:1 line and the solid blue and orange lines are the binned mean and median, respectively, calculated on bins containing equal numbers of data points. Binned mean and median are also calculated on the 95% confidence levels of ε, resulting in the confidence intervals shown here.

perhaps explaining why the confidence intervals for bin-means in Figure 5a overlap with the former but not the latter. Figure 5b shows the binned median, but not mean, of ε plotted against B_0 to overlap with Equation 21. As alluded to by the factor ~5 difference in overall mean and median (Table 2), the scaling of ε by B_0 appears to have a number of extreme outliers that skew the mean high, arguably making the median the more representative statistic in this specific case. Lastly, binned averages of ε plotted against $\frac{u_s u_*^2}{h}$ in the wind-dominant regime, which does not account for Langmuir turbulence, fall along the 1:1 line except for a large deviation for values of $\frac{u_s u_*^2}{h} < 10^{-7}$ (Figure 5c). This is corrected when it is applied in the Langmuir-dominant regime defined by $\frac{h}{L_L}$ (Figure 6c).

4.4. Sensitivity of Scaling to *La*

The calculated statistics for $\frac{u_*^3}{\kappa z}$ and B_0 vary relatively little between regimes defined using $\frac{z}{L_M}$ versus $\frac{h}{L_L}$ (Tables 2 and 3) and binned means and medians appear largely similar across Figures 5 and 6, suggesting that the distinction between regimes defined by $\frac{z}{L_M}$ and those defined by $\frac{h}{L_L}$ is somewhat unimportant in the Stratus region. This is tied to the low variability of *La* across most of the study period (Figure 3): Because $L_M \propto La^2 L_L$, largely constant values of *La* result in a linear dependency between L_L and L_M, shown in Figure 7. Figure 8 shows ε scaled by Equation 21, calculated from binned values of $\frac{u_*^3}{\kappa z}$ and B_0, in *La* space. Scaling by Equation 21 removes variability tied to B_0 and u_*, so if Langmuir effects were not sufficiently accounted for by $\frac{u_*^3}{\kappa z}$, we would expect to see a large deviation from unity at lower values of *La*, where Langmuir forcing is stronger. Instead, there is very little variability in *La* space, suggesting that *La* offers little to no additional predictive power over u_* at this field site.

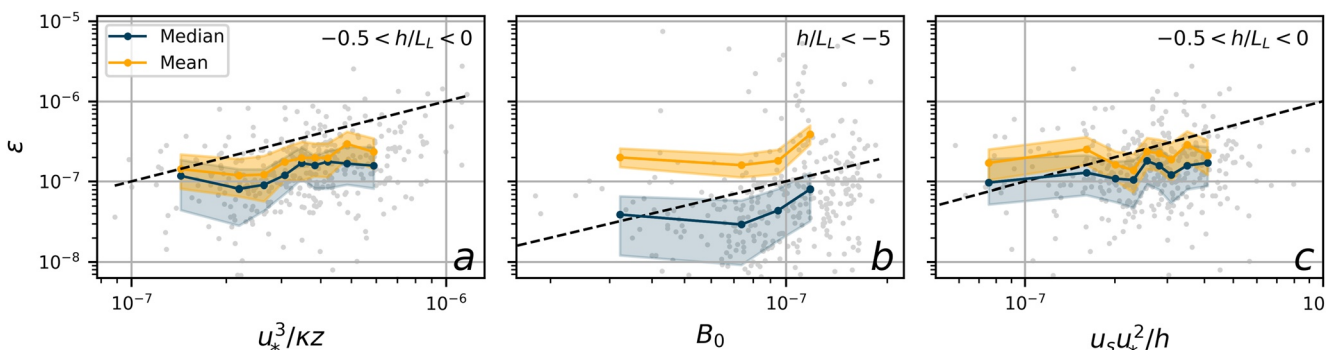

Figure 6. Same as Figure 5 but with regimes defined by $\frac{h}{L_L} < -0.5$ (buoyancy-dominant regime) and $\frac{h}{L_L} > -5$ (Langmuir-dominant regime).
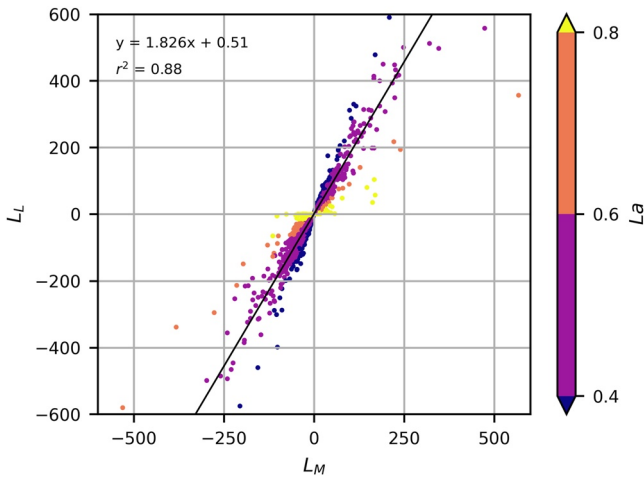
Figure 7. Least squares linear regression of L_L (Equation 11) with L_M (Equation 5), illustrating the relationship $L_M \propto La^{-2}L_L$. Colors highlight the variation in slope associated with different values of binned La (Equation 10).

Furthermore, for ε scaled by $\frac{u_*^3}{\kappa z}$, we see little change in calculated statistics in the Langmuir-dominant regime in both destabilizing and stabilizing conditions when data coinciding with lower La values are excluded (Table 4). The median of scaled ε increases slightly from 0.4 to 0.54 in destabilizing conditions and remains ~0.3 in stabilizing conditions, regardless of the degree of exclusion. In destabilizing conditions, the mean increases as more data are excluded, but only because the influence of several outlying data points on the mean is strengthened with increasingly fewer data points.

5. Discussion

The Stratus region is characterized by directionally-steady southeast trade winds (Weller et al., 2014), which likely contribute to the observed linear relationship between u_s and u_* and an overall narrow range in La across the study period. The stronger the relationship between u_s and u_*, the more functionally equivalent w_{*L} and u_* become, a concept noted by Gargett and Grosch (2014). Therefore, at the Stratus mooring site, there appears to be little need to distinguish between wind- and Langmuir-dominant regimes in the context of turbulence scaling. We see a strong linear relationship between L_M and L_L and little difference in the scaling of ε by $\frac{u_*^3}{\kappa z}$ and B_0 in regimes defined by $\frac{h}{L_L}$ compared to $\frac{z}{L_M}$ (Tables 2 and 3). The mean, median, and interquartile range of $\frac{\varepsilon \kappa z}{u_*^3}$ are nearly identical across $\frac{h}{L_L}$ and $\frac{z}{L_M}$ wind- and Langmuir-dominant regimes in both destabilizing and stabilizing conditions, as are the statistics for $\frac{\varepsilon}{B_0}$ for both of the buoyancy-dominant regimes in destabilizing conditions. As the Stratus region is known to lack synoptic forcing and exhibit relative uniformity in hydrographic surveys and wind fields, results from data collected at the mooring site are considered applicable over large swaths of the Stratus region (Holte et al., 2014; Weller et al., 2014). It is important to note that while our analysis shows that ε scaling is not sensitive to the La regime, this does not mean that Langmuir circulation/turbulence is unimportant in the Stratus region, only that it is sufficiently accounted for by u_* due to the linear relationship between u_* and u_s. Regardless, the ability to consider wind- and Langmuir-dominant regimes as equivalent, irrespective of La, is useful and
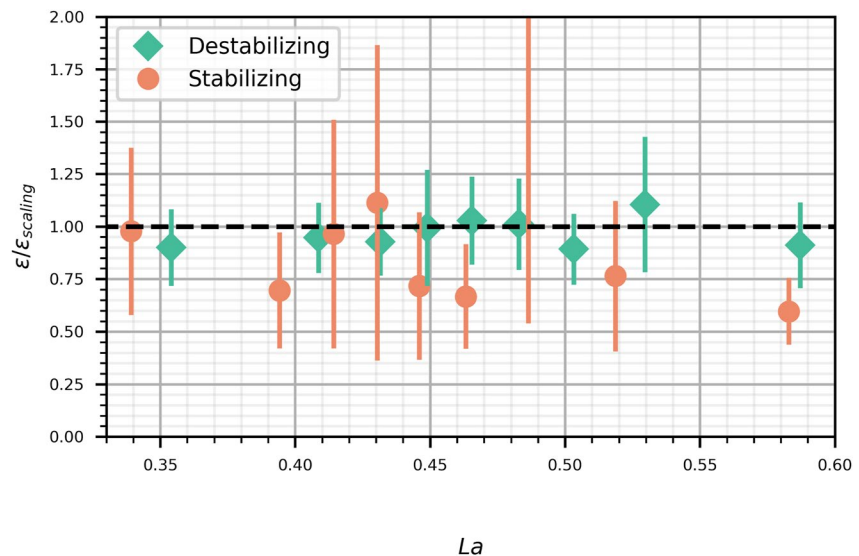

Figure 8. Bin-averaged measurements of ε (away from the top and bottom of the mixed layer; $\mathbf{0.135 < \frac{z}{h} < 0.5}$) scaled by Equation 21 in destabilizing conditions and $u_*^3/\kappa z$ in stabilizing conditions across La space. Because Equation 21 was fitted to data in which the highest and lowest 1% of values were excluded, the same filter is applied to the data in destabilizing conditions shown here. Each bin contains the same number of points. Vertical bars show the 95% confidence interval, calculated as 1.96 multiplied by the standard error, of scaled ε in each bin.

Table 4

Median, Mean, and Interquartile Range (Q75–Q25) Calculated for ε Scaled by $u_*^3/\kappa z$ Where Subsets of Data Defined Using the Langmuir Number La, Are Excluded in Order to Explore the Distinction Between Langmuir and Current Shear-Forced Regimes in Our Data

$\varepsilon z \kappa / u_*^3$			
	Excluding $La < 0.4$	Excluding $La < 0.45$	Excluding $La < 0.5$
$B_0 > 0,\ \left|\frac{h}{L_L}\right| < 0.5$			
N	400	300	167	59
Median	0.40	0.42	0.44	0.54
Mean	0.67	0.72	0.82	1.26
Q75–Q25	0.50	0.51	0.52	0.60
$B_0 < 0,\ \left|\frac{h}{L_L}\right| < 0.5$			
N	175	132	77	38
Median	0.35	0.34	0.29	0.29
Mean	0.61	0.67	0.66	0.68
Q75–Q25	0.49	0.49	0.54	0.72

Note. Only data that fall away from the top and bottom of the mixed layer ($0.135 < \frac{z}{h} < 0.5$) are considered.

may be relevant in efforts to improve the performance of ocean models in this region. It may also be broadly applicable to turbulence scaling outside of the steadily-forced Stratus region: in a study of dissipation rates from microstructure profiler deployments at several sites ranging from the Arctic Ocean to the subtropical Atlantic Ocean, Esters et al. (2018) found that the observed linear relationship between u_* and u_s allowed them to describe their data using a version of Equation 13 in which u_s is substituted by u_* multiplied by a constant factor.

In wind- and Langmuir-dominant regimes across both destabilizing and stabilizing conditions, we observe $\frac{u_*^3}{\kappa z}$ to collapse the scatter of ε and scale it to an average of ∼0.65. The scaling of ε close to, but not exactly, unity is common in observational studies. Callaghan et al. (2014) observed periods of both systematic underestimation (e.g., average $\frac{\varepsilon \kappa z}{u_*^3}$ ranging from 1.21 to 1.84 across several depths) and overestimation (e.g., 0.59–0.74) of ε by LOW, speculating that the former could be the result of Langmuir turbulence and the latter due to a continually changing wind direction in which a misalignment of the wind and wave field reduced the effective wind stress on the ocean. Tedford et al. (2014) attributed overestimation by LOW (average $\frac{\varepsilon \kappa z}{u_*^3} = 0.52$ in destabilizing conditions, 0.62 in stabilizing) in a lake setting to enhanced stratification brought on by the lateral advection of cool water. Lombardo and Gregg (1989) observed an average $\frac{\varepsilon \kappa z}{u_*^3}$ of 1.76 in destabilizing conditions and suggested that the underestimation was likely due to the contributions of convective turbulence. Esters et al. (2018) similarly found averages of 0.85 in stabilizing conditions and 1.72 in destabilizing conditions.

Variation about unity by a factor of 1–2 is consistent with the findings of Moum et al. (1995), who attributed disparities of a roughly factor of 2 between measurements of ε at two field sites to natural variability in turbulence, that is, the intermittent nature of turbulent flows and spatial and temporal variation between measurements. However, as most studies noted, systematic under- or overestimation of ε can result from the influence of processes not accounted for by the scaling. We explore possible sources of systematic bias in our own data here:

Near-Inertial Oscillations

The Stratus region exhibits periodic dips in wind speeds that have been observed to generate near-inertial oscillations capable of altering currents and potentially impacting the turbulence regime through the generation of additional current shear (Weller et al., 2014). In Figure 2, some of these periods of low wind speeds are seen to correspond with instances where LOW drastically underestimates measurements of ε, such as in mid-February and throughout June. However, there are also instances of dips in wind speeds where LOW does track the drop in measured ε, such as in mid-January and mid-April, and Figure 5a shows that mean agreement between measured ε and $\frac{u_*^3}{\kappa z}$ is actually closer to 1:1 at lower wind speeds (corresponding to smaller values of u_*), indicating the impact of these dips in wind is minimal and that underestimation of ε is instead systematic across all wind speeds.

Suppression of Current Shear by Langmuir Circulation

LES studies have shown the enhancement of vertical mixing associated with Langmuir circulation reduces vertical shear in the upper ocean, inhibiting current shear production of TKE (Belcher et al., 2012; Fan et al., 2020) and therefore reducing the magnitude of ε relative to $\frac{u_*^3}{\kappa z}$. While Figure 3 would suggest a nearly year-round influence of Langmuir turbulence at the Stratus mooring site, it is difficult to gauge how much of an impact the suppression of vertical shear would have on LOW in a real ocean setting; Lombardo and Gregg (1989) visibly observed Langmuir wind streaks during the several of their microstructure profiler deployments but noted no systematic departure of ε measurements from similarity scaling.

Instrument Noise Floor

In a comparison of mooring-based ADCP measurements of ε with those derived from a microstructure shear probe deployed on a nearby glider, Zippel et al. (2021) found the mooring-based measurements to be mostly biased high below values of $\varepsilon = 10^{-8}\,\text{W}\,\text{kg}^{-1}$. They noted that $10^{-8}\,\text{W}\,\text{kg}^{-1}$ is the energy level below which the ratio of instrument noise variance, estimated from ping correlation values (Zippel et al., 2021; Equation 7 and references therein), to total spectral variance becomes large, resulting in a higher sensitivity of the fit of Equation 15 to noise term, N. This increasing influence of noise at low energy levels may be the reason why we observe slightly higher binned means and medians of ε relative to $\frac{u_*^3}{\kappa z}$ at lower energy levels near $10^{-8}\,\text{W}\,\text{kg}^{-1}$ than at higher energy levels (Figures 5 and 6). While this source of bias in low energy settings is important to acknowledge in any turbulence study involving pulse-coherent ADCPs, it would not contribute to the systematic overestimation of ε by $\frac{u_*^3}{\kappa z}$ in question here; instead it would contribute to an underestimation because it biases ε high, not low, relative to $u_*^3/\kappa z$. Furthermore, it would contribute to discrepancies from LOW only at low energy levels rather than the overestimation observed across all energy levels in Figures 5a and 6a.

Anisotropy

Stratification can suppress vertical turbulence and break the assumption of isotropy implicit in Equation 14. It has been shown that the balance between local production and dissipation of TKE breaks down in anisotropic conditions (Scully et al., 2011), as inferred from the Ozmidov scale ($L_{oz} = \varepsilon^{\frac{1}{2}}/N^{\frac{3}{2}}$; N here is buoyancy frequency rather than instrument noise), which represents the upper bound of the length scale for vertical turbulence in a stratified flow. Zippel et al. (2021) suggested that anisotropy could contribute to the observed high-bias in their ADCP-based measurements of ε at energy levels below $10^{-8}\,\text{W}\,\text{kg}^{-1}$, finding that an L_{oz} consistent with the $\sim 1\,\text{m}$ sampling profile length of the ADCP corresponded to values of ε of the magnitude $10^{-8}\,\text{W}\,\text{kg}^{-1}$. Because ADCPs measure the inertial subrange rather than scales closer to the Kolmogorov range, their spectra are more sensitive than those of shear probes to the Ozmidov scale rolloff. This could be further compounded by the horizontal orientation of our ADCP sampling profile, which would perhaps capture more horizontally-oriented eddies than buoyancy-limited vertically-oriented eddies, resulting in an overestimation of ε in anisotropic conditions. However, as with the instrument noise floor discussed in Section 5.3, anisotropy cannot explain the observed overestimation of ε by LOW as it would contribute to a high-bias in ε, rather than a low-bias.

Assumption of a Constant Stress Layer

MOST and LOW rely on the assumption of constant stress. Observations (Gerbi et al., 2008) and linear surface stress scaling (e.g., Fisher et al., 2017) show stress to decay with depth according to $\tau_z = \tau\left(1 - \frac{z}{h}\right)$, suggesting LOW calculated from τ at the surface would overestimate shear turbulence at depth. When calculating LOW using decayed stress, τ_z, our measurements of ε (within the same $0.135 < \frac{z}{h} < 0.5$ range as before) are scaled with averages of 1.28 and 1.01 where $\left|\frac{h}{L_L}\right| < 0.5$ and 0.95 and 1.04 where $\left|\frac{z}{L_M}\right| < 0.3$, in destabilizing and stabilizing conditions, respectively. These values are notably closer to unity than ~ 0.65. There is little reason to assume the constant stress layer assumption holds at the 8.4 m depth of our measurements, and these calculations suggest that stress decay may be a factor in the systematic underestimation of ε by $\frac{u_*^3}{\kappa z}$ in real-world conditions.

While turbulence is complex and we are unable to conclusively determine the cause of the systematic deviation from LOW, the decay of stress with depth seems likely to play a contributing role. Nevertheless, our results are on par with averages obtained in prior studies and support the merit of classic MOST despite a possible violation of the constant stress layer assumption. Future work is needed to more fully assess if full flux-profile relationships are tenable outside of the constant stress layer, but within the OBL.

The $\frac{u_s u_*^2}{h}$ scaling has not been widely examined outside of modeling studies because of the difficulty in obtaining quality wave data concurrently with in-situ measurements of ε. That $\frac{u_s u_*^2}{h}$ appears to scale ε closer to unity for much of November-April (Figure 2a) is perhaps surprising, as this scaling is a relatively new development

(Grant & Belcher, 2009) and limited observational studies of the TKE budget have disagreed on the magnitude of the Stokes production term relative to the dissipation term (Gerbi et al., 2009; Jarosz et al., 2021; Yoshikawa et al., 2018). Regardless, by June, the wind-sea weakens (monthly-averaged H_{sw} is 0.86 m compared to ~1.2 m across the whole study period) and the scaling grossly underestimates ε. Filtering out values of $H_{sw} < 1$ m, as well as $U_{10} < 5$ m s^{-1} and $u_s < 0.03$ m s^{-1}, which would coincide with conditions of weak Langmuir forcing, does not systemically separate instances of significant underestimation of ε by $\frac{u_s u_*^2}{h}$ from instances where it performs well. Given that our results show u_* to implicitly capture the effects of Langmuir turbulence, $\frac{u_*^3}{\kappa z}$ serves as a more reliable scaling for ε in wind- and Langmuir-dominant regimes, as its overestimation bias is fairly consistent and more easily corrected for.

As for the B_0 scaling, scatter is collapsed in destabilizing, buoyancy-dominant conditions, but ε is overestimated by an average of ~2.5. The median of ~0.6 is closer to unity and the averages reported in other studies, such as ~0.58 in Lombardo and Gregg (1989) and 0.81 in Anis and Moum (1992). The large difference between the mean and the median indicates that the mean is influenced by extreme outliers, which can be seen in Figure 5b. These outliers are likely present because the Stratus mooring site does not experience true buoyancy-dominant conditions, which are typically defined by values of $\frac{z}{L_M} < -5$ (Zippel et al., 2021) or $\frac{z}{L_M} < 10$ (Lombardo & Gregg, 1989). To retain a sufficient number of data points, we defined a less conservative threshold of $\left| \frac{z}{L_M} \right| < 3$, which would increase the influence of turbulent processes not captured by B_0. Nevertheless, as with the mean values of $\frac{\varepsilon \kappa z}{u_*^3}$, the median values of $\frac{\varepsilon}{B_0}$ are on par with those of previous studies and similarly support the use of MOST in the Stratus region in destabilizing conditions.

Scaling relationships in MOST are useful as they allow us to describe ε across a continuous range of $\frac{z}{L_M}$ and can be tuned to fit observations. In destabilizing conditions, the majority of scaling relationships from prior studies align fairly well with Equation 20 and the binned mean of $\frac{\varepsilon \kappa z}{u_*^3}$ where $\frac{z}{L_M} > -1$, suggesting that MOST is broadly applicable to a variety of boundary layer settings in this regime. The scaling relationship of Lombardo and Gregg (1989) may differ from the other aquatic studies (Figure 4) because it utilized a descending microstructure profiler that necessarily omitted data 5 m near the surface, possibly excluding surface wave-related turbulence otherwise captured in our data and studies utilizing ascending profilers. Likewise, the scaling relationships of Wyngaard and Coté (1971) may deviate from the other relationships because they were derived from data collected in the ABL above a wheat field. The other ABL study considered here, Edson and Fairall (1998), was conducted in the marine ABL where wave activity may have had an influence. Regardless, all of the relationships deviate from the binned mean of our data in destabilizing conditions of $\frac{z}{L_M} < -2$. This could be because in general, fewer data exist at greater values of $\left| \frac{z}{L_M} \right|$, making statistics and linear regressions derived from these data less universal. Furthermore, scaling relationship with coefficients derived from the scaling of ε measurements by $\frac{u_*^3}{\kappa z}$ and B_0 ostensibly describe turbulence from wind-driven current shear and convection, but inadvertently capture the effects of many other processes that are potentially unique to the place and time of data collection, with the intermittent nature of turbulence adding additional complexity. Data collected in studies using microstructure profilers represent snapshots in time and are therefore perhaps more susceptible to this temporal and spatial variability, possibly contributing to the spread in scaling relationships derived from field estimates of ε.

In stabilizing conditions, MOST appears much less applicable to our data. The lack of variability in $\frac{\varepsilon \kappa z}{u_*^3}$ with $\frac{z}{L_M}$ demonstrates a much weaker influence of stabilizing buoyancy flux than suggested by the ABL scaling relationships of Edson and Fairall (1998) and Wyngaard and Coté (1971) (Figure 4). While it would be simple to attribute this discrepancy to inherent differences between the ABL and OBL, we note that Tedford et al. (2014) fit a scaling relationship of the form of Equation 7 to data in a lake surface boundary layer that is similarly divergent from our data (not shown). In general, the applicability of MOST in the OBL under stabilizing conditions is much less explored than in destabilizing conditions, and would be a worthwhile focus for future studies.

Turbulence is key in processes such the subduction of heat and climate-relevant gasses into the ocean interior (Belcher et al., 2012) and the redistribution of phytoplankton, zooplankton, and nutrients (Tedford et al., 2014). It is therefore useful to be able to estimate ε across time and turbulence regimes. While turbulence is inherently noisy and complex, we have found that $\frac{u_*^3}{\kappa z}$, B_0, and MOST scaling relationships can sufficiently predict
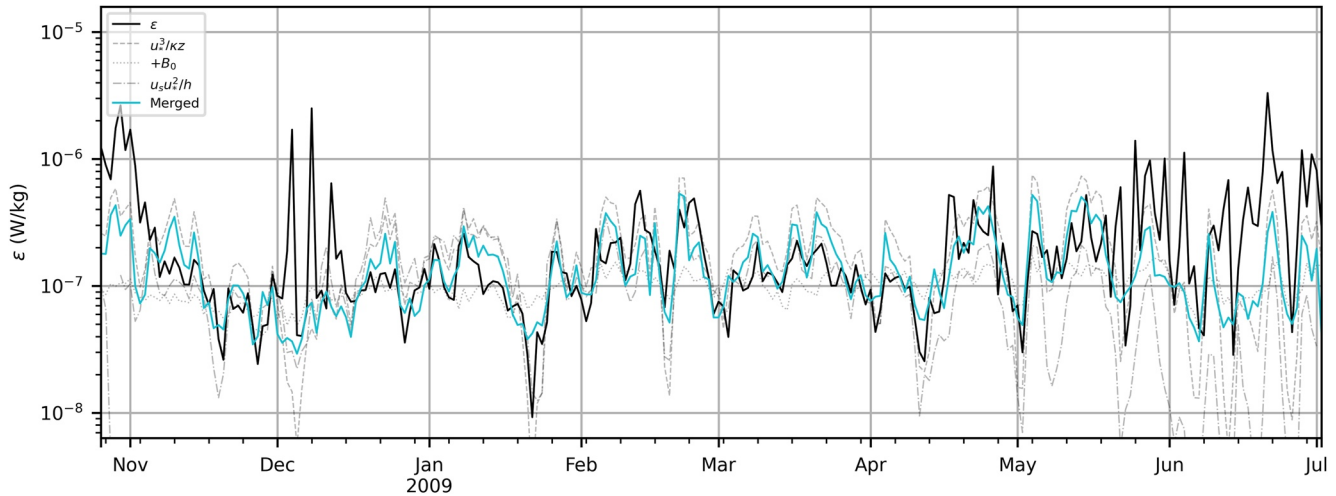
Figure 9. The same daily-averaged time series of ε and $\frac{u_*^3}{\kappa z}$, B_0, and $u_s u_*^2/h$ shown in Figure 2a, now overlaid with a "merged scaling" that applies $u_*^3/\kappa z$ where $\frac{z}{L_M} > 0$, B_0 where $\frac{z}{L_M} < -1$, and Equation 21 where $-1 < \frac{z}{L_M} < 0$.

bin-averaged values of ε across various ranges of $\frac{z}{L_M}$. We apply daily-averaged $\frac{u_*^3}{\kappa z}$, B_0, and Equation 21 in the following regimes:

$$\varepsilon = \begin{cases} B_0 & where\ \dfrac{z}{L_M} < -1 \\ 0.69 u_*^3/\kappa z - 0.46 B_0 & where -1 < \dfrac{z}{L_M} < 0 \\ u_*^3/\kappa z & where\ \ \dfrac{z}{L_M} > 0 \end{cases}$$

These scalings are shown as a single, merged time series in Figure 9, overlying the daily-averaged time series of ε measurements and Equation 2 scaling relationships originally shown in Figure 2a. The ratio of daily-averaged ε to daily-averaged $\frac{u_*^3}{\kappa z}$ and the merged scalings are 1.3 and 1.0, respectively. By taking into account various turbulence regimes as defined by $\frac{z}{L_M}$, the merged scalings are better able to capture the magnitude of ε, demonstrating the utility of MOST.

6. Conclusion

Moored, pulse-coherent ADCP measurements of ε are a useful development in the study of ocean turbulence, allowing for analysis of turbulence across an extended range of conditions and length of time at a single site. Here, we have used similarity scaling to explore 9 months of moored measurements of ε across a range of forcing conditions in the OBL of the Stratus region. We find that:

- $\frac{u_*^3}{\kappa z}$ scales ε to ~ 0.65 where $\left|\frac{z}{L_M}\right| < 0.3$, a value close to unity consistent with LOW and on par with the findings of previous studies
- B_0 scales ε to ~ 0.6 where $\frac{z}{L_M} < -3$, also on par with previous studies
- $\frac{u_s u_*^2}{h}$ scales ε close to unity for a large portion of the study period, but scales ε very poorly in May and June. It is difficult to parse out the conditions in which it performs well, therefore $\frac{u_*^3}{\kappa z}$ remains the more useful scaling in wind-dominant conditions
- $\frac{h}{L_L}$ and $\frac{z}{L_M}$ are functionally equivalent means for separating the wind- and Langmuir-dominant regimes from the buoyancy-dominant regime in the Stratus region because of the strong linear relationship between u_* and u_s

- Prior scaling relationships largely agree with our measurements in destabilizing conditions where $\frac{z}{L_M} > -1$, but their deviation where $\frac{z}{L_M} < -1$ and in stabilizing conditions highlights how field estimates of ϵ are susceptible to variability across space and time

- A combination of $u_*^3/\kappa z$, B_0, and Equation 21, applied where $\frac{z}{L_M} > 0$, $\frac{z}{L_M} < -1$, and $-1 < \frac{z}{L_M} < 0$, respectively, is able to reproduce daily-averaged time series measurements of ϵ better in terms of magnitude than any single scaling alone

Conflict of Interest

The authors declare no conflicts of interest relevant to this study.

Data Availability Statement

Velocity, correlation, amplitude, and other outputs from the 2 MHz Nortek AquaDopp High-Resolution (HR) Pulse-Coherent ADCP are available from https://doi.org/10.7916/xs7h-b561. Processed dissipation rates and other calculated variables (such as B_0 and u_s used in the analyses are available from https://doi.org/10.7916/ypkn-x736. Meteorological measurements and other data from the Stratus Ocean Reference Station are made freely available by the OceanSITES project (Send et al., 2010) and the national programs that contribute to it, and may be obtained from https://dods.ndbc.noaa.gov/oceansites/. Wave data from the mooring are hosted by the National Buoy Data Center and are obtained from https://www.ndbc.noaa.gov/station_page.php?station=32012. The MATLAB code used to quality control the ADCP data and calculate ϵ (Zippel et al., 2021) is available on GitHub at https://github.com/zippelsf/MooredTurbulenceMeasurements. The MATLAB code used to calculate Stokes drift was written by Dr. Adrean Webb and is available through the MATLAB File Exchange (Webb, 2022). The Gibbs-SeaWater Oceanographic toolbox (McDougall & Barker, 2011) is downloadable from http://www.teos-10.org/software.htm#1 and the COARE bulk flux algorithm (Fairall et al., 1996, 2003) from https://github.com/NOAA-PSL/COARE-algorithm.

References

Agrawal, Y. C., Terray, E. A., Donelan, M. A., Hwang, P. A., Iii, A. J. W., Drennan, W. M., et al. (1992). Enhanced dissipation of kinetic energy beneath surface waves. *Nature*, *359*(6392), 359219a0–220. https://doi.org/10.1038/359219a0

Anis, A., & Moum, J. N. (1992). The superadiabatic surface layer of the ocean during convection. *Journal of Physical Oceanography*, *22*(10), 1221–1227. https://doi.org/10.1175/1520-0485(1992)022<1221:tsslot>2.0.co;2

Anis, A., & Moum, J. N. (1995). Surface wave–turbulence interactions. Scaling ε(z) near the sea surface. *Journal of Physical Oceanography*, *25*(9), 2025–2045. https://doi.org/10.1175/1520-0485(1995)025<2025:swisnt>2.0.co;2

Belcher, S. E., Grant, A. L. M., Hanley, K. E., Fox-Kemper, B., Roekel, L. V., Sullivan, P. P., et al. (2012). A global perspective on Langmuir turbulence in the ocean surface boundary layer. *Geophysical Research Letters*, *39*(18). https://doi.org/10.1029/2012GL052932

Brainerd, K. E., & Gregg, M. C. (1993). Diurnal restratification and turbulence in the oceanic surface mixed layer: 1. Observations. *Journal of Geophysical Research*, *98*(C12), 22645–22656. https://doi.org/10.1029/93JC02297

Callaghan, A. H., Ward, B., & Vialard, J. (2014). Influence of surface forcing on near-surface and mixing layer turbulence in the tropical Indian Ocean. *Deep-Sea Research Part A Oceanographic Research Papers*, *94*, 107–123. https://doi.org/10.1016/j.dsr.2014.08.009

Colbo, K., & Weller, R. A. (2009). Accuracy of the IMET sensor package in the subtropics. *Journal of Atmospheric Oceanic Technology*, *26*(9), 1867–1890. https://doi.org/10.1175/2009JTECHO667.1

Craig, P. D., & Banner, M. L. (1994). Modeling wave-enhanced turbulence in the ocean surface layer. *Journal of Physical Oceanography*, *24*(12), 2546–2559. https://doi.org/10.1175/1520-0485(1994)024<2546:MWETIT>2.0.CO;2

Craik, A. D. D., & Leibovich, S. (1976). A rational model for Langmuir circulations. *Journal of Fluid Mechanics*, *73*(3), 401–426. https://doi.org/10.1017/S0022112076001420

D'Asaro, E. A. (2014). Turbulence in the upper-ocean mixed layer. *Annual Review of Marine Science*, *6*(1), 101–115. https://doi.org/10.1146/annurev-marine-010213-135138

Drennan, W. M., Kahma, K. K., Terray, E. A., Donelan, M. A., & Kitaigorodskii, S. A. (1992). Observations of the enhancement of kinetic energy dissipation beneath breaking wind waves. In *Breaking waves, international union of theoretical and applied mechanics* (pp. 95–101). Springer. https://doi.org/10.1007/978-3-642-84847-6_6

Edson, J., Crawford, T., Crescenti, J., Farrar, T., Frew, N., Gerbi, G., et al. (2007). The coupled boundary layers and air–sea transfer experiment in low winds. *Bulletin of the American Meteorological Society*, *88*(3), 341–356. https://doi.org/10.1175/BAMS-88-3-341

Edson, J. B., & Fairall, C. W. (1998). Similarity relationships in the marine atmospheric surface layer for terms in the TKE and scalar variance budgets. *Journal of Atmospheric Oceanic Technology*, *55*(13), 2311–2328. https://doi.org/10.1175/1520-0469(1998)055<2311:sritma>2.0.co;2

Esters, L., Breivik, Ø., Landwehr, S., Ten Doeschate, A., Sutherland, G., Christensen, K. H., et al. (2018). Turbulence scaling comparisons in the ocean surface boundary layer. *Journal of Geophysical Research: Oceans*, *123*(3), 2172–2191. https://doi.org/10.1002/2017JC013525

Fairall, C. W., Bradley, E. F., Hare, J. E., Grachev, A. A., & Edson, J. B. (2003). Bulk parameterization of air–sea fluxes: Updates and verification for the COARE algorithm. *Journal of Climate*, *16*(4), 571–591. https://doi.org/10.1175/1520-0442(2003)016<0571:bpoasf>2.0.co;2

Fairall, C. W., Bradley, E. F., Rogers, D. P., Edson, J. B., & Young, G. S. (1996). Bulk parameterization of air-sea fluxes for tropical ocean-global atmosphere coupled-ocean atmosphere response experiment. *Journal of Geophysical Research Oceans*, *101*(C2), 3747–3764. https://doi.org/10.1029/95JC03205

Fan, Y., Yu, Z., Savelyev, I., Sullivan, P. P., Liang, J.-H., Haack, T., et al. (2020). The effect of Langmuir turbulence under complex real oceanic and meteorological forcing. *Ocean Modelling*, *149*, 101601. https://doi.org/10.1016/j.ocemod.2020.101601

Fisher, A. W., Sanford, L. P., Scully, M. E., & Suttles, S. E. (2017). Surface wave effects on the translation of wind stress across the air–sea interface in a fetch-limited, coastal embayment. *Journal of Physical Oceanography*, *47*(8), 1921–1939. https://doi.org/10.1175/JPO-D-16-0146.1

Gargett, A. E., & Grosch, C. E. (2014). Turbulence process domination under the combined forcings of wind stress, the Langmuir vortex force, and surface cooling. *Journal of Physical Oceanography*, *44*(1), 44–67. https://doi.org/10.1175/JPO-D-13-021.1

Gemmrich, J. R., & Farmer, D. M. (2004). Near-surface turbulence in the presence of breaking waves. *Journal of Physical Oceanography*, *34*(5), 1067–1086. https://doi.org/10.1175/1520-0485(2004)034<1067:NTITPO>2.0.CO;2

Gerbi, G. P., Trowbridge, J. H., Edson, J. B., Plueddemann, A. J., Terray, E. A., & Fredericks, J. J. (2008). Measurements of momentum and heat transfer across the air–sea interface. *Journal of Physical Oceanography*, *38*(5), 1054–1072. https://doi.org/10.1175/2007JPO3739.1

Gerbi, G. P., Trowbridge, J. H., Terray, E. A., Plueddemann, A. J., & Kukulka, T. (2009). Observations of turbulence in the ocean surface boundary layer: Energetics and transport. *Journal of Physical Oceanography*, *39*(5), 1077–1096. https://doi.org/10.1175/2008JPO4044.1

Grant, A. L. M., & Belcher, S. E. (2009). Characteristics of Langmuir turbulence in the ocean mixed layer. *Journal of Physical Oceanography*, *39*(8), 1871–1887. https://doi.org/10.1175/2009JPO4119.1

Holte, J., Straneo, F., Farrar, J. T., & Weller, R. A. (2014). Heat and salinity budgets at the stratus mooring in the southeast Pacific. *Journal of Geophysical Research: Oceans*, *119*(11), 8162–8176. https://doi.org/10.1002/2014JC010256

Hwang, P. A., Ocampo-Torres, F. J., & García-Nava, H. (2011). Wind sea and swell separation of 1D wave spectrum by a spectrum integration method. *Journal of Atmospheric Oceanic Technology*, *29*(1), 116–128. https://doi.org/10.1175/JTECH-D-11-00075.1

Jarosz, E., Wijesekera, H. W., & Wang, D. W. (2021). Coherent velocity structures in the mixed layer: Characteristics, energetics, and turbulent kinetic energy budget. *Journal of Physical Oceanography*, *51*, 2991–3014. https://doi.org/10.1175/JPO-D-20-0248.1

Kitaigorodskii, S. A., Donelan, M. A., Lumley, J. L., & Terray, E. A. (1983). Wave-turbulence interactions in the upper ocean. Part II. Statistical characteristics of wave and turbulent components of the random velocity field in the marine surface layer. *Journal of Physical Oceanography*, *13*(11), 1988–1999. https://doi.org/10.1175/1520-0485(1983)013<1988:WTIITU>2.0.CO;2

Kolmogorov, A. (1941). The local structure of turbulence in incompressible viscous fluid for very large Reynolds' numbers. *Akademii Nauk SSSR Doklady*, *30*, 301–305.

Leibovich, S. (1983). The form and dynamics of Langmuir circulations. *Annual Review of Fluid Mechanics*, *15*(1), 391–427. https://doi.org/10.1146/annurev.fl.15.010183.002135

Lenain, L., & Pizzo, N. (2020). The contribution of high-frequency wind-generated surface waves to the Stokes drift. *Journal of Physical Oceanography*, *50*(12), 3455–3465. https://doi.org/10.1175/JPO-D-20-0116.1

Li, Q., & Fox-Kemper, B. (2017). Assessing the effects of Langmuir turbulence on the entrainment buoyancy flux in the ocean surface boundary layer. *Journal of Physical Oceanography*, *47*(12), 2863–2886. https://doi.org/10.1175/JPO-D-17-0085.1

Li, Q., Reichl, B. G., Fox-Kemper, B., Adcroft, A. J., Belcher, S. E., Danabasoglu, G., et al. (2019). Comparing ocean surface boundary vertical mixing schemes including Langmuir turbulence. *Journal of Advances in Modeling Earth Systems*, *11*, 3545–3592. https://doi.org/10.1029/2019MS001810

Lin, J.-L. (2007). The double-ITCZ problem in IPCC AR4 coupled GCMs: Ocean–atmosphere feedback analysis. *Journal of Climate*, *20*(18), 4497–4525. https://doi.org/10.1175/JCLI4272.1

Lombardo, C. P., & Gregg, M. C. (1989). Similarity scaling of viscous and thermal dissipation in a convecting surface boundary layer. *Journal of Geophysical Research*, *94*(C5), 6273–6284. https://doi.org/10.1029/JC094iC05p06273

Ma, C.-C., Mechoso, C. R., Robertson, A. W., & Arakawa, A. (1996). Peruvian stratus clouds and the tropical Pacific circulation: A coupled ocean-atmosphere GCM study. *Journal of Climate*, *9*(7), 1635–1645. https://doi.org/10.1175/1520-0442(1996)009<1635:PSCATT>2.0.CO;2

McDougall, T. J., & Barker, P. M. (2011). *Getting started with TEOS-10 and the Gibbs seawater (GSW) oceanographic toolbox* (pp. 28). SCOR/IAPSO WG127.

McWilliams, J. C., Sullivan, P. P., & Moeng, C.-H. (1997). Langmuir turbulence in the ocean. *Journal of Fluid Mechanics*, *334*, 1–30. https://doi.org/10.1017/S0022112096004375

Mechoso, C. R., Robertson, A. W., Neelin, J. D., Davey, M., Delecluse, P., Gent, P., et al. (1995). The seasonal cycle over the tropical Pacific in coupled ocean-atmosphere general circulation models. *Monthly Weather Review*, *123*(9), 2825–2838. https://doi.org/10.1175/1520-0493(1995)123<2825:TSCOTT>2.0.CO;2

Monin, A. S., & Obukhov, A. M. (1959). Basic laws of turbulent mixing in the surface layer of the atmosphere.

Moum, J. N., Gregg, M. C., Lien, R. C., & Carr, M. E. (1995). Comparison of turbulence kinetic energy dissipation rate estimates from two ocean microstructure profilers. *Journal of Atmospheric Oceanic Technology*, *12*(2), 346–366. https://doi.org/10.1175/1520-0426(1995)012<0346:COTKED>2.0.CO;2

Paulson, C. A., & Simpson, J. J. (1977). Irradiance measurements in the upper ocean. *Journal of Physical Oceanography*, 7(6), 952–956. https://doi.org/10.1175/1520-0485(1977)007<0952:IMITUO>2.0.CO;2

Price, J. F., Weller, R. A., & Pinkel, R. (1986). Diurnal cycling: Observations and models of the upper ocean response to diurnal heating, cooling, and wind mixing. *Journal of Geophysical Research*, *91*(C7), 8411–8427. https://doi.org/10.1029/JC091iC07p08411

Richter, I. (2015). Climate model biases in the eastern tropical oceans: Causes, impacts and ways forward. *WIREs Climate Change*, *6*(3), 345–358. https://doi.org/10.1002/wcc.338

Schneider, W., Fuenzalida, R., Rodríguez-Rubio, E., Garcés-Vargas, J., & Bravo, L. (2003). Characteristics and formation of Eastern South Pacific intermediate water. *Geophysical Research Letters*, *30*(11), 1581. https://doi.org/10.1029/2003GL017086

Scully, M. E., Geyer, W. R., & Trowbridge, J. H. (2011). The influence of stratification and nonlocal turbulent production on estuarine turbulence: An assessment of turbulence closure with field observations. *Journal of Physical Oceanography*, *41*(1), 166–185. https://doi.org/10.1175/2010JPO4470.1

Send, U., Weller, R. A., Wallace, D. W. R., Chavez, F., Lampitt, R. L., Dickey, T., et al. (2010). OceanSITES. *Proceedings of oceanObs'09: Sustained ocean observations and information for society*. In J. Hall, D. E. Harrison, & D. Stammer (Eds.), ESA Publication WPP-306, Venice, Italy, 21-25 September 2009. https://doi.org/10.5270/OceanObs09.cwp.79

Shay, T. J., & Gregg, M. C. (1986). Convectively driven turbulent mixing in the upper ocean. *Journal of Physical Oceanography*, *16*(11), 1777–1798. https://doi.org/10.1175/1520-0485(1986)016<1777:CDTMIT>2.0.CO;2

Soloviev, A., & Lukas, R. (2003). Observation of wave-enhanced turbulence in the near-surface layer of the ocean during TOGA COARE. *Deep-Sea Research Part A Oceanographic Research Papers*, *50*(3), 371–395. https://doi.org/10.1016/S0967-0637(03)00004-9

Sreenivasan, K. R. (1995). On the universality of the Kolmogorov constant. *Physics of Fluids*, *7*(11), 2778–2784. https://doi.org/10.1063/1.868656

Stips, A., Burchard, H., Bolding, K., Prandke, H., Simon, A., & Wüest, A. (2005). Measurement and simulation of viscous dissipation in the wave affected surface layer. *Deep Sea Research Part II: Topical Studies in Oceanography*, *52*(9–10), 1133–1155. https://doi.org/10.1016/j.dsr2.2005.01.012

Stull, R. B. (1988). *An introduction to boundary layer meteorology, Atmospheric sciences library*. Kluwer Academic Publishers.

Sutherland, G., Christensen, K. H., & Ward, B. (2014). Evaluating Langmuir turbulence parameterizations in the ocean surface boundary layer. *Journal of Geophysical Research: Oceans*, *119*(3), 1899–1910. https://doi.org/10.1002/2013JC009537

Sutherland, P., & Melville, W. K. (2015). Field measurements of surface and near-surface turbulence in the presence of breaking waves. *Journal of Physical Oceanography Boston*, *45*(4), 943–965. https://doi.org/10.1175/jpo-d-14-0133.1

Tedford, E. W., MacIntyre, S., Miller, S. D., & Czikowsky, M. J. (2014). Similarity scaling of turbulence in a temperate lake during fall cooling. *Journal of Geophysical Research: Oceans*, *119*(8), 4689–4713. https://doi.org/10.1002/2014JC010135

Teng, C.-C., Bernard, L., Taft, B., & Burdette, M. (2005). A compact wave and ocean data buoy system. *Proceedings of oceans 2005 MTS/IEEE. Presented at the Proceedings of Oceans 2005 MTS/IEEE*, *2*, 1249–1254. https://doi.org/10.1109/OCEANS.2005.1639926

Terray, E. A., Donelan, M. A., Agrawal, Y. C., Drennan, W. M., Kahma, K. K., Williams, A. J., et al. (1996). Estimates of kinetic energy dissipation under breaking waves. *Journal of Physical Oceanography*, *26*(5), 792–807. https://doi.org/10.1175/1520-0485(1996)026<0792:EOKEDU>2.0.CO;2

Van Roekel, L. P., Fox-Kemper, B., Sullivan, P. P., Hamlington, P. E., & Haney, S. R. (2012). The form and orientation of Langmuir cells for misaligned winds and waves. *Journal of Geophysical Research*, *117*(C5). https://doi.org/10.1029/2011JC007516

Veron, F., & Melville, W. K. (1999). Pulse-to-pulse coherent Doppler measurements of waves and turbulence. *Journal of Atmospheric Oceanic Technology*, *16*(11), 1580–1597. https://doi.org/10.1175/1520-0426(1999)016<1580:PTPCDM>2.0.CO;2

Wang, D. W., & Hwang, P. A. (2001). An operational method for separating wind sea and swell from ocean wave spectra. *Journal of Atmospheric Oceanic Technology*, *18*(12), 2052–2062. https://doi.org/10.1175/1520-0426(2001)018<2052:AOMFSW>2.0.CO;2

Webb, A. (2022). Stokes drift for directional random seas. MATLAB Central file exchange. Retrieved from https://www.mathworks.com/matlabcentral/fileexchange/48678-stokes-drift-for-directional-%20random-seas

Webb, A., & Fox-Kemper, B. (2015). Impacts of wave spreading and multidirectional waves on estimating Stokes drift. *Ocean Modelling, Waves and Coastal, Regional and Global Processes*, *96*, 49–64. https://doi.org/10.1016/j.ocemod.2014.12.007

Weller, R. A. (2015). Variability and trends in surface meteorology and air–sea fluxes at a site off Northern Chile. *Journal of Climate*, *28*(8), 3004–3023. https://doi.org/10.1175/JCLI-D-14-00591.1

Weller, R. A., Majumder, S., & Tandon, A. (2014). Diurnal restratification events in the southeast Pacific trade wind regime. *Journal of Physical Oceanography*, *44*(9), 2569–2587. https://doi.org/10.1175/JPO-D-14-0026.1

Wood, R., Mechoso, C. R., Bretherton, C. S., Weller, R. A., Huebert, B., Straneo, F., et al. (2011). The VAMOS ocean-cloud-atmosphere-land study regional experiment (VOCALS-REx): Goals, platforms, and field operations. *Atmospheric Chemistry and Physics*, *11*(2), 627–654. https://doi.org/10.5194/acp-11-627-2011

Wyngaard, J. C., & Coté, O. R. (1971). The budgets of turbulent kinetic energy and temperature variance in the atmospheric surface layer. *Journal of Atmospheric Science*, *28*(2), 190–201. https://doi.org/10.1175/1520-0469(1971)028<0190:TBOTKE>2.0.CO;2

Yoshikawa, Y., Baba, Y., Mizutani, H., Kubo, T., & Shimoda, C. (2018). Observed features of Langmuir turbulence forced by misaligned wind and waves under destabilizing buoyancy flux. *Journal of Physical Oceanography*, *48*(11), 2737–2759. https://doi.org/10.1175/JPO-D-18-0038.1

Zheng, Y., Shinoda, T., Lin, J.-L., & Kiladis, G. N. (2011). Sea surface temperature biases under the stratus cloud deck in the Southeast Pacific Ocean in 19 IPCC AR4 coupled general circulation models. *Journal of Climate*, *24*(15), 4139–4164. https://doi.org/10.1175/2011JCLI4172.1

Zippel, S. F., Farrar, J. T., Zappa, C. J., Miller, U., Laurent, L. S., Ijichi, T., et al. (2021). Moored turbulence measurements using pulse-coherent Doppler sonar. *Journal of Atmospheric Oceanic Technology*, *38*, 1621–1639. https://doi.org/10.1175/JTECH-D-21-0005.1

Zuidema, P., Chang, P., Medeiros, B., Kirtman, B. P., Mechoso, R., Schneider, E. K., et al. (2016). Challenges and prospects for reducing coupled climate model SST biases in the eastern tropical Atlantic and Pacific Oceans: The U.S. CLIVAR eastern tropical oceans synthesis working group. *Bulletin of the American Meteorological Society*, *97*(12), 2305–2328. https://doi.org/10.1175/BAMS-D-15-00274.1

Erratum

In the originally published version of this article, the term "LOW" in Equation 21 was used instead of the form "$\frac{u_*^3}{\kappa z}$", which is used in equations 3 and 8 as well as throughout the main text of the article. The error has been corrected, and this may be considered the authoritative version of record.